Metal-Insulator-Metal thin film stack: flux enhancement due to coupling of surface plasmon polariton with wave guide modes

Georges Raşeev, Moustafa Achlan

Journal of Physics D: Applied Physics

ACCEPTED MANUSCRIPT

MIM thin film stack: flux enhancement due to coupling of surface plasmon polariton with wave guide modes

To cite this article before publication: Georges Raseev *et al* 2020 *J. Phys. D: Appl. Phys.* in press https://doi.org/10.1088/1361-6463/abb103

Metal-Insulator-Metal thin film stack: flux enhancement due to coupling of surface plasmon polariton with wave guide modes

Georges Raşeev*and Moustafa Achlan
Université Paris-Saclay, Univ. Paris-Sud, CNRS, Institut des Sciences Moléculaires d'Orsay, 91405 Orsay, France

August 17, 2020

Abstract

An theoretical study is presented of the dispersion of surface plasmon polariton (SPP) and wave guide (WG) modes of a metal-insulator-metal (MIM) thin film stack. We study the dispersion of the reflectance and of the transmitted flux, originating from a local excitation source, of an asymmetric MIM air-Au-SiO_2-Au-Ti-glass material system in the infrared and visible spectral region for a wide range of SiO_2 and gold thicknesses, d_{SiO_2} and d_{Au}. In comparison to reference stacks of air-Au-glass or air-SiO_2-glass, between 1.4 and 2.0 eV, the transmitted flux intensity is enhanced 12 or 25 times, in the emission direction of the in-plane wave vector $k_\rho/k_0 \approx$1.05 and for a thickness of $d_{SiO_2} \in$[300-700] nm, respectively. This enhancement is attributed to the coupling, through the avoided crossings, between the SPP_{air} and WG modes. As the fields of the SPP_{air} and WG modes are located in different regions of space the enhancement is nearly independent of the number of nodes in the WG mode. In summary we have identified sets of parameters giving rise to the observables enhancement. Therefore the present MIM thin film stack is a simple and a versatile system for the use in applications.

1 Introduction

The surface plasmon polaritons (SPP) are coherent longitudinal surface fluctuations of an electron plasma at an interface between two media, usually metal-dielectric, coupled to an external electromagnetic field. The SPP give rise to an enhancement of this electromagnetic field [1]. This enhancement is now studied in involved geometrical structures with interfaces including flat and corrugated thin films stacks, films with ridges, stripes, wedges, single particles and holes and periodically structured arrays ([2, 3]). The applications of the field enhancement and other optical phenomena in these structures are numerous in microelectronic circuitry, radiative decay [3, 4], wave guides [5], organic plasmon emitting diode [6] and chemical and biological sensors [7].

In the literature, flat multi-layered thin film stacks containing metals come in two configurations: the insulator-metal-insulator (IMI) [8, 9, 10, 11, 12, 13] and the metal-insulator-metal (MIM) [14, 15, 16, 17, 18, 19]. Both types of stack have been studied widely with both experimental and theoretical approaches. In an experiment, a variety of optical measurements can be performed: attenuated total reflection (ATR) ([12, 20, 21]), reflectance and fluorescence [22], angular resolved photoluminescence [23] and angular resolved electron energy loss [24]. In the case of near-field probe techniques, the AFM [5] or STM [25] tip provides a localized source of excitation. The transmitted flux intensity and any enhancement that may occur, is measured. Applications are numerous, in particular for flat stacks. In MIM stacks the SPP-WG (wave guide) modes coupling can be exploited [14, 15] while in IMI stacks having a spacer, they display a sharp Fano resonance of use in sensors using monochromatic [8, 9] or radial polarized white light [22].

A theoretical approach to studying these stacks involves solving the analytical expression of the dispersion for both complex in-plane and out-of-plane wave vector projections k_ρ and k_z ([13, 19, 26, 27]). Another approach is to first calculate a 3D plot where the abscissas correspond to the real ω/k_ρ or ω/k_z

*corresponding author, e-mail: georges.raseev@universite-paris-saclay.fr

variables and the ordinate to the observable intensity. Then the 2D ω/k_ρ and ω/k_z plots of the observable extrema permit the dispersion curves to be drawn ([28, 25, 22, 18, 20, 29, 30, 31]).

For $IMI_1 ... I_n$ stacks Ditlbacher *et al.* [12] studied the dispersion of the modes in a glass-SU8-Ag-SiO_2-air-prism system and identified an avoided crossing between the SPP-WG modes. More recently, Hayashi, Nesterenko, Sekat and co-workers measured the reflectance in an ATR set-up in stacks composed of air-(DR1 doped poly(methyl methacrylate) or PMMA)-Cytop(spacer)-Ag-prism(SF11) [30], air-(DR1 doped PMMA)-Cytop(spacer)-Ag-prism(SF10) [32], and air-Al_2O_3-SiO_2-Al-SF11-prism(SF11) [11]. At λ=632.8 nm (ω=1.9593 eV) the reflectance/incident angle graph displays an extremely steep Fano resonance of interest in sensor applications.

SPP and WG modes have been identified in systems with claddings other than glass ; for example, water in a water-Cytop-I-Au-prism stack where Cytop is a spacer and 'I' is ZnS+SiO_2 ref. [29, 33] or PMMA ([34]). Again at λ=632.8 nm the reflectance/incident angle graph displays a Fano resonance that is very sensitive to changes of the refractive index in a solution containing a chemical or a biological system to be analyzed [7, 15, 8, 9].

The organic plasmon emitted diode, another application of IMI stacks, was initially developed using only thin film stacks [35], though now the thin films are combined with nano structures [6].

The Ag-I-Ag and Ag-I_1-I_2-Ag MIM thin film stacks have been studied by Hayashi and co-workers [21, 23, 31] using photoluminescence and ATR. By measuring the photoluminescence in an air-Ag-MgF_2-Alq_3-MgF_2-Ag-glass stack and comparing it to calculations, Hayashi *et al.* [23] found an avoided crossing between the plasmonic air-Ag SPP and photonic WG modes. The photoluminescence enhancement can be compared with a metal-free stack or with a single metal and dielectric stack of the MI or IM type. In a particular emission direction this enhancement can be as much as 25 times larger than that of a metal-free stack. Integrating over the light emission angle to obtain the electromagnetic local density of states (EM-LDOS) gives rise to an enhancement of 2.5. Yang *et al.* [17] found a modest few percent enhancement of $E_{\parallel}^2$ in a study comparing air-Au(200 nm)-SiO_2(50 nm)-Al_2O_3(50 nm)-Au(200 nm)-air and air-Au(200 nm)-SiO_2(100 nm)-Au(200 nm)-air stacks.

Verhagen *et al.* [5] found air-Ag SPP and MIM-SPP modes in their study of a MIM air-Ag-Si_3N_4-Ag stack excited by an AFM tip. Since the intensity of the field in the dielectric is large it is probable that their MIM-SPP mode is a SPP-WG hybrid mode. For a MIM air-Ag-PMMA-Ag-BK6(prism) thin film stack Refki *et al.* [31] measured the ATR minimum at different wavelengths to obtain an experimental dispersion curve in good agreement with the theoretical dispersion derived from power dissipation calculations. They found that the position of the avoided crossing changes with the dielectric thickness and the avoided crossing strength rises as the silver thickness diminishes. Again the assignment of the Ag-air SPP mode seems correct whereas the S-SPP mode is probably a hybrid SPP-WG mode. Using an air-Ag-SiO_2-Au-SiO_2-(quart prism) thin film stack Neo *et al.* [16] measured the ATR function of the incident angle at λ=632.8 nm and performed calculations using a finite-difference time-domain (FDTD) model. For two thicknesses of the stack they identified a sharp Fano resonance. Using a He-lamp (590-670 nm) and a He-Ne laser at λ=632.8 nm Matsunaga *et al.* [36] studied the reflectance of an air-Ag-SiO_2-Au-quartz prism. Their reflectance-incident angle graphs present a wide and a narrow feature, that they attributed to the WG and the SPP modes, respectively. They also identified a Fano resonance.

To estimate the usefulness of MIM sensors using water Refki *et al.* [14] performed an ATR experiment at λ=632.8 nm to study a water-Au-PMMA-Ag-prism thin film stack in which a sharp Fano resonance was identified. By using the figure of merit they were able to qualify this stack as a possible sensor to measure the change of the refractive index in solution. Recently Vlcek *et al.* [15] proposed to combine MIM and IMI stacks ((rutile-prism)-Au-glass-Au and (rutile-prism)-(air gap)-(gallium-gadolinium garnet)-(bismuth-doped gadolinium iron garnet)-(aqueous solution)) in an effort to develop new sensors based on reflectance changes for the analysis of the constituents of an aqueous solution.

The papers discussed above show that in an IMI or a MIM thin film stack the sustained modes can produce resonance phenomena and the enhancement of the observables. Often the cited experimental and theoretical studies considered thin film stacks of fixed thickness and wavelength.

What are the best geometrical parameters, laser frequencies and in-plane wave vectors able to give rise to observable enhancements and resonances and produce tools of use in applications? In this paper we will try to answer these questions in a theoretical study of the light emission from a metal-insulator-metal (MIM) stack Au-SiO_2-Au where the thickness of the two layers of gold is identical and the cladding is composed of air and glass resulting in an asymmetric air-Au-SiO_2-Au-Ti-glass thin film stack. The idea is to model a stack of the same type as the one studied in Cao *et al.* [25] and investigate new sets of parameters permitting the enhancement of the transmitted flux in this stack. To be precise, in this work we have calculated the dispersion of our gold MIM stack from 3D plots where the ordinates are the reflectance $\mathcal{R}$ and the locally excited transmitted flux $S^{\downarrow}$. In this work we have systematically varied the thicknesses of the insulator and metal films ($d_{\mathrm{SiO_2}} \in [100, 800]$ and $d_{\mathrm{Au}} \in [10, 60]$ nm), the excitation energies, $\hbar\omega(\mathrm{eV}) \in [0.7, 4.3]$ covering the surface plasmon polariton (SPP), quasi bound (QB) and radiative plasmon polariton (RPP) photon domains, and the in-plane wave vector k_ρ ($k_\rho/k_0 \in [0, 1.52]$, with $k_0 = \omega/c$ and n_{glass}=1.52).

We show that above the surface plasmon (SP) resonance at 2.384 eV the observable amplitudes are weak, consequently our study is confined to the region below this SP resonance. Compared to reference stacks composed of air-Au-glass or air-SiO_2-glass, the transmitted flux intensity is enhanced by a factor 12 or 22, respectively. The EM-LDOS, integrated over the in-plane wave vector flux is enhanced by about 2.5. The observables enhancement originates from the $\mathrm{SPP_{air}}$-WG avoided crossing instead of the leakage of the SPP mode. Since the fields of the $\mathrm{SPP_{air}}$ and the WG modes are located in different regions of space, this enhancement takes place at few SiO_2 thicknesses in the domain $d_{\mathrm{SiO_2}} \in [200, 700]$ nm.

In summary in this study we have identified sets of parameters giving rise to the enhancement of the observables. Therefore the present MIM thin film stack is a simple and a versatile system for the use in applications.

2 Observables and simple models

2.1 Reflectance and transmitted flux from a local excitation

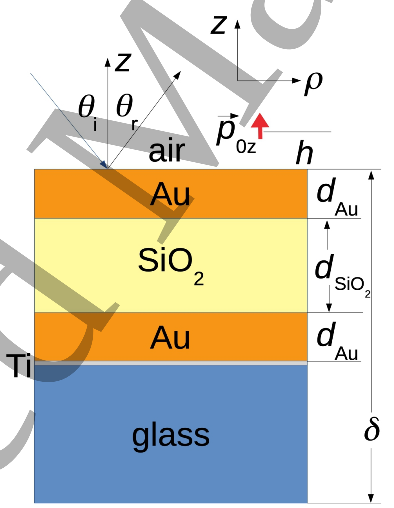

Figure 1: Schematic representation of the six-layer asymmetric MIM stack air-Au-SiO_2-Au-Ti-glass. The two excitation modes are presented above the top air-Au interface : i) the $\mathfrak{p}$ polarized plane wave photon (upper left); ii) a vertical oscillating dipole $\vec{\mathrm{p}}_{0z}$ located at a height h, a few nm above the first interface, a local excitation (upper right). The cylindrical system of coordinate $\{z, \rho, \varphi\}$ used here is represented in the upper right corner.

Figure 1 presents the air-Au-SiO_2-Au-Ti-glass six-layer asymmetric thin film stack similar to the one studied experimentally by Cao *et al.* [25]. The excitation occurs either through a plane wave $\mathfrak{p}$ polarized photon incident on the surface at an angle θ_i with the reflectance measured at the reflection angle θ_r (upper left corner). Or by a vertical oscillating dipole $\vec{\mathrm{p}}_{0z}$ located at a height h a few nm above the surface (upper right corner). In this work two projections are used: i) the in-plane projection corresponding to the $\{\rho, \varphi\}$ plane, in the momentum space k_ρ, and ii) the out-of-plane projection, in the momentum space k_z.

The observables presented below for the $\mathfrak{p}$ polarized light will be used to calculate the dispersion of our MIM thin film stack. The reflectance $\mathcal{R}$ is a ratio of the reflected and incident Poynting vectors $\vec{S}$

projections on the normal to the surface $\vec{n} \equiv z$ (Yeh [37, chapter 3])

$$\mathcal{R}^{(\mathfrak{p})}(\theta_i, \omega) = \frac{\vec{S}^{(r)} \cdot \vec{n}}{\vec{S}^{(i)} \cdot \vec{n}} = [r^{(\mathfrak{p})}]^2, \qquad \vec{S} = \vec{E} \times \vec{H}^*, \tag{1}$$

where $r^{(\mathfrak{p})}$ is the Fresnel reflection coefficient in $(\mathfrak{p})$/TM polarization. The multiple reflections and refractions of all the layers of the stack are included in this term. We implemented the transfer matrix algorithm of Abèles-Bethune [38] using the method explained in Achlan's PhD thesis [28, chapter 5] and in Cao *et al.* [25, appendix]. In the rest of the paper we will use the notation $\mathcal{R} \equiv \mathcal{R}^{(\mathfrak{p})}$.

For a local excitation by a vertical oscillating dipole $\vec{p}_{0z}$ located at a height h a few nm above the top interface (see figure 1), only the $\mathfrak{p}$/TM polarized light contributes to the transmitted flux or Poynting vector $S_n^{\downarrow}$. For a stack of n layers one writes ([28, 25, 39, 40, 41, 42])

$$\begin{aligned} S_n^{\downarrow}(k_\rho, \delta, \omega) &= S_{na}^{\downarrow}(k_\rho, \delta, \omega) + S_{nf}^{\downarrow}(k_\rho, \delta, \omega) \\ S_{na}^{\downarrow}(k_\rho, \delta, \omega) &= \frac{p_{0z}^2}{64\,\pi^2} \frac{c^2\,k_\rho^2}{\omega\,\varepsilon_0} \frac{t_{1n}^{(\mathfrak{p})}(k_\rho, \delta)}{(k_{1z}/k_0)} \left(\frac{k_{nz}\,t_{1n}^{(\mathfrak{p})}(k_\rho, \delta)}{(k_{1z}/k_0)} \right)^* & k_\rho \in [0, k_1] \\ S_{nf}^{\downarrow}(k_\rho, \delta, \omega) &= \frac{p_{0z}^2}{64\,\pi^2} \frac{c^2\,k_\rho^2}{\omega\,\varepsilon_0} \frac{t_{n1}^{(\mathfrak{p})}(k_\rho, \delta)}{(k_{1z}/k_0)} \left(\frac{k_{nz}\,t_{n1}^{(\mathfrak{p})}(k_\rho, \delta)}{(k_{1z}/k_0)} \right)^* \exp(-2\,k_{1z}^{"}\,h) & k_\rho \in (k_1, k_n], \end{aligned} \tag{2}$$

where $k_{1z}^{"}$ is the imaginary part of k_{1z}. The above expressions are written in cylindrical coordinates with k_ρ and k_z the in-plane and the out-of-plane projections of the wave vector where δ is the thickness of the entire thin film stack (see figure 1). Here $t_{1n}^{(p)}$ and $t_{n1}^{(p)}$ are the Fresnel transmission coefficients through the entire stack (1 to n and n to 1 layers) including all the reflections and refractions with the plane wave excitation from the first and the last medium. The quantities $S_{na}^{\downarrow}$ and $S_{nf}^{\downarrow}$ are the allowed 'a' and forbidden 'f' or evanescent contributions to the transmitted flux intensity or the Poynting vector in the last substrate layer n. Further details on the model and its implementation can be found in refs. [28, 25].

How one can measure the enhancement in a MIM thin film stack? As proposed by Hayashi *et al.* [23] and Yang *et al.* [17] the enhancement is evaluated by calculating the ratio of the transmitted fluxes in the present stack compared to a reference stack. The obvious choice for a reference stack is either **(i)** a dielectric stack, in this case air-SiO_2-glass or **(ii)** a insulator-metal-insulator (IMI) stack, in this case air-Au-glass, respectively the Poynting vectors ${}^{\mathrm{aSiO_2g}}S_n^{\downarrow}$ or ${}^{\mathrm{aAug}}S_n^{\downarrow}$.

Consider first the maximum flux of our six-layer MIM stack ${}^{\mathrm{MIM}}S_n^{\downarrow}$ given eq. (2) above. At a particular frequency ω and a gold thickness d_{Au} this maximum is obtained by varying k_ρ and SiO_2 thickness $d_{\mathrm{SiO_2}}$ up to the optimal values k_ρ^{max} and δ^{max}=$2d_{\mathrm{Au}}$+$d_{\mathrm{SiO_2}}$ (max means a parameter value corresponding to the maximum of ${}^{\mathrm{MIM}}S_n^{\downarrow}$). Then at k_ρ^{max} and δ^{max} one calculates the reference stack flux ${}^{ref}S_n^{\downarrow}$. Now $I_{ref}(\omega)$, the ratio of these two fluxes, reads

$$I_{ref}(\omega) = \frac{S^{\downarrow}(k_\rho^{max}, \delta^{max}, \omega)}{S_{ref}^{\downarrow}(k_\rho^{max}, \delta^{max}, \omega)} = \frac{[S^{\downarrow}(k_\rho, \delta, \omega)]_{max}}{S_{ref}^{\downarrow}(k_\rho^{max}, \delta^{max}, \omega)}, \tag{3}$$

expression written using a simplified notation $S^{\downarrow} \equiv {}^{\mathrm{MIM}}S_n^{\downarrow}$ and $S_{ref}^{\downarrow} \equiv {}^{ref}S_n^{\downarrow}$, notation also used in the rest of the paper. For the air-Au-glass stack the gold thickness is ${}^{\mathrm{aAug}}d_{\mathrm{Au}} = 2\left({}^{MIM}d_{\mathrm{Au}}\right)$. What happens if in eq. (3) one uses an optimized reference flux $\{S_{ref}^{\downarrow}\}_{max}$? We have performed calculations comparing both expressions; the results are reasonably close so that a separate evaluation is not needed.

2.2 Simple models for plasmonic SPP and photonic WG modes

Simple analytical models, presented in the appendix A, give the characteristic properties either of the SPP mode at a single interface or of the WG mode for a three-layer stack. These models permit an analysis of the modes sustained in our six layers stack. In summary:

- Section A.1 discusses the dispersion of the plasmon polariton (PP) modes of gold and silver at a metal-dielectric interface that appear in the SPP, QB and RPP spectral regions. These regions cover respectively the $\hbar\omega \in [\omega_{min}, \omega_{sp}]$, $\hbar\omega \in [\omega_{sp}, \omega_{rpp}]$ and $\hbar\omega \in [\omega_{rpp}, \omega_{max}]$ spectral domains.

The first and second columns of figures A-1 and A-2 present the dispersion and the leakage of the gold-air and silver-air interfaces. The dispersion curves of the $\mathrm{PP_{air}}$ and the $\mathrm{PP_{glass}}$ modes are located at $\mathrm{Re}[k_\rho/k_0] \approx 1$ and $\mathrm{Re}[k_\rho/k_0] \approx 1.52$. They are well separated in gold but in silver they sweep and cross over the entire domain of wave vector projections. The second row of figures A-1 and A-2 show that below the SP resonance $\hbar\omega \in [\omega_{min}, \omega_{sp}]$ the leakage is extremely low in gold and silver for both in-plane $|\mathrm{Im}[k_\rho/k_0]| \ll 0.1$ and out-of-plane $|\mathrm{Im}[k_z/k_0]| \ll 0.1$ wave vector projections ($\pm$ sign or proper/improper Riemann sheet in equations (A-1) and (A-2)).

- Section A.2 discusses the photonic WG modes in an Au-SiO_2-Au stack. The left and middle panels of figure A-3 show the real n^r_{Au} and imaginary κ_{Au} parts of the refractive index of the gold as a function of the frequency. The condition of the appearance of the WG modes, i.e. $n^r_{\mathrm{Au}} < n_{\mathrm{SiO_2}}$ ($n_{\mathrm{SiO_2}} \approx$1.5), is fulfilled for $\hbar\omega(\mathrm{eV}) \in [0.65, 2.5]$. Our calculations were performed using a simple accumulated phase model valid for dielectrics discussed in Saleh and Teich [43, section 7.2] where the phase φ_z is calculated using the complex refractive index of gold. The results presented in figure A-4 show that, as expected, the number of nodes per energy unit rises with the SiO_2 thickness.

It appears that the above independent calculations of the SPP and WG modes locate their appearance in the same spectral and wave vector region. Then in the MIM stack studied here, these modes will interact giving rise to avoided crossings particularly since in the studied frequency region the gold skin depth is between 25-40 nm comparable to this layer thickness $d_{\mathrm{Au}} \in$[15-40] nm (see figure A-3, third panel).

3 Results

3.1 Reflectance and transmitted flux spectra of the SPP and WG modes

This section presents the spectra of the reflectance $\mathcal{R}$ (eq. (1)) and of the transmitted flux intensity $S^{\downarrow}$ (eq. (2)) obtained on an asymmetric glass-Au-SiO_2-Au-Ti-air thin film stack (see figure 1) in the optical region as a function of the in-plane wave vector k_ρ/k_0. We study the entire optical domain $\hbar\omega(\mathrm{eV}) \in [0.7, 4.3]$ covering three spectral regions; the SPP ($\hbar\omega \in [\omega_{min}, \omega^{\mathrm{Au}}_{sp}$), the QB ($\hbar\omega \in [\omega^{\mathrm{Au}}_{sp}, \omega^{\mathrm{Au}}_{rpp}]$) and the RPP ($\hbar\omega \in [\omega^{\mathrm{Au}}_{rpp}, \omega_{max}]$), where ω_{min} =0.7 eV, ω_{max} =4.3 eV, $\omega^{\mathrm{Au}}_{sp}$=2.384 eV and $\omega^{\mathrm{Au}}_{rpp}$=3.3715 eV. The in-plane wave vector $k_\rho/k_0 \in [0, 1.52]$ corresponds to the experimental measurements of the transmission flux in glass performed by Cao *et al.* [25]. The results presented below are the raw calculations which are analyzed in the rest of the paper.

Figure 2 presents a top view of the 3D plots of the reflectance $\mathcal{R}$ function of $k_\rho/k_0 \in$[0.7,1.3] (columns 1 and 3) and of the transmitted flux $S^{\downarrow}$ function of $k_\rho/k_0 \in [0.98, 1.3]$ (columns 2 and 4) in the restricted frequency domain $\hbar\omega(\mathrm{eV}) \in [0.7, 2.8]$. In these observables, the PP and WG modes appear respectively as minima and maxima. Figures B-1 and B-2 of appendix B present these same observables in the extended frequency domain $\hbar\omega(\mathrm{eV}) \in [0.7, 4.3]$. Above the SP resonance at $\omega^{\mathrm{Au}}_{sp}$=2.384 eV the extrema of the modes become so weak that they are barely distinguishable from the background. Consequently in the rest of the paper we restrict our study to a region slightly wider than the SPP spectral region, namely $\omega \in [0.7, 2.8]$ eV.

The 3D graphs of these three figures (2, B-1 and B-2) display possible $\mathrm{SPP_{air}}$-WG avoided crossings and the comparison with the uncoupled representation of $\mathrm{SPP_{air}}$ and WG modes shown in figure 3 validates this interpretation.

In figures 2 and 3 two in-plane wave vector k_ρ/k_0 regions can be distinguished:

- The **allowed** region, where the in-plane wave vector is $k_\rho/k_0 \in [0, 1]$. In this region we only present the reflectance (columns 1 and 3 of figure 2) since the transmitted flux $S^{\downarrow}$ has an extremely low maximum. In figure 3 and in columns 1 and 3 of figure 2 the WG modes are nearly independent of frequency ω. As in the uncoupled representation of figure 3, when increasing the SiO_2 thickness the reflectance $\mathcal{R}$ is able to sustain an increasing number of WG modes per frequency unit (columns 1 and 3 of figure 2). Therefore we tentatively identify these modes weakly dependent on frequency with the WG modes having a different number of nodes ℓ.
- The **forbidden or evanescent** region with $k_\rho/k_0 \in [1, 1.52]$. In the uncoupled representation of figure 3 several crossings between a $\mathrm{SPP_{air}}$ and WG modes are present whereas the $\mathrm{SPP_{glass}}$ is located

above k_ρ/k_0 >1.52 (see section A.1) beyond the in-plane wave vector domain studied here. In the 3D graphs presented in figure 2 these SPP_{air}-WG crossings become avoided with the splitting governed by the extent of the interaction between the modes. By continuity with the allowed region and by comparing with the uncoupled representation of figure 3 the WG and SPP modes are identified in both observables.

The second and fourth columns of figure 2 show that, when varying the parameters of our MIM stack in the forbidden region, one observes an enhancement in $S^{\downarrow}$ of between 2 and 8 10^{-6} for d_{Au}=25, 40 nm and $d_{\mathrm{SiO}_2} \in$[300,800] nm. This enhancement will be discussed further in section 3.4 below. When the in-plane wave vector $k_\rho/k_0 < 1.0$ or $k_\rho/k_0 > 1.3$ one is far from the avoided crossing and the transmitted flux intensity $S^{\downarrow}$ is weak.

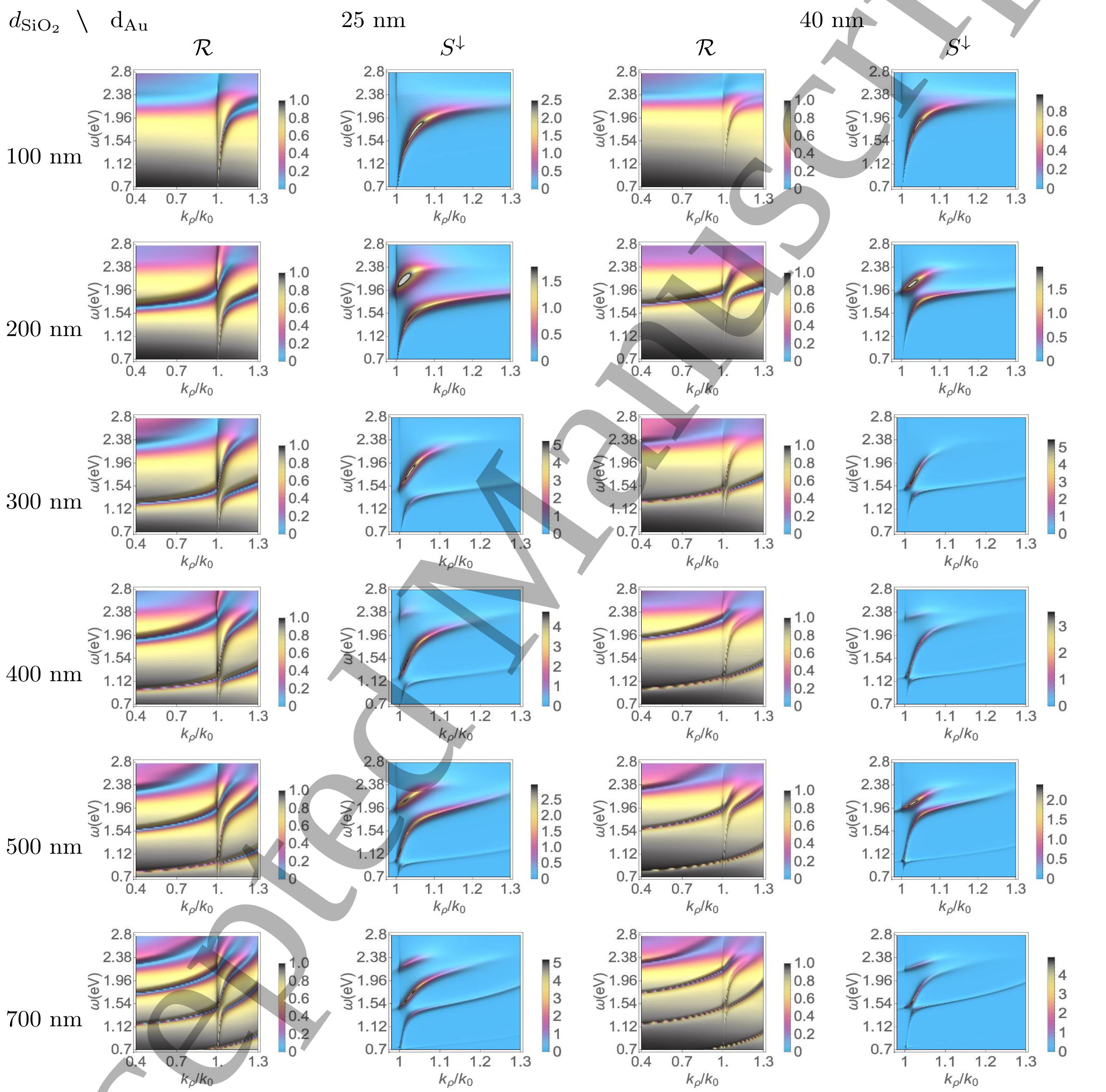

Figure 2: Top view of the 3D plots of the MIM thin film stack (figure 1) reflectance $\mathcal{R}$ (columns 1 and 3, abscissa $k_\rho/k_0 \in$[0.4,1.3]) and of the transmitted flux intensity $S^{\downarrow}$ (columns 2 and 4, abscissa $k_\rho/k_0 \in$[0.9,1.3]) in the energy domain $\hbar\omega$(eV) $\in$[0.7,2.8]. Rows and columns correspond to the SiO_2 and Au thicknesses.

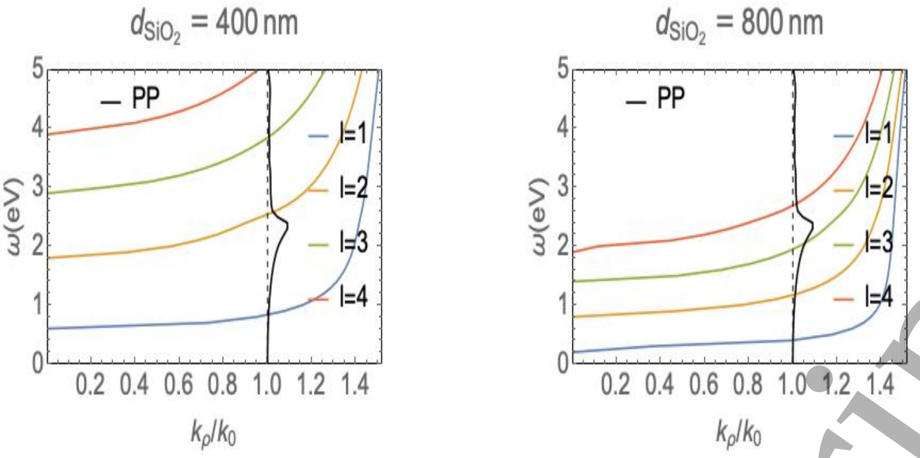

Figure 3: Uncoupled representation of dispersion curves: **(i)** black curve taken from fig. A-1 corresponds to a plasmon polariton (PP) mode at the air-Au interface and in air. Below $\hbar\omega_{sp}$ <2.384 eV this PP becomes a SPP_{air} mode; **(ii)** color curves correspond to WG modes with $\ell \in [1, 4]$ of an Au-SiO_2-Au stack are taken from fig. A-4. The left and the right panels show the thickness d_{SiO_2} =400 and 800 nm respectively. The dashed vertical line separates the allowed (left) and the forbidden (right) spectral regions.

Finally consider the evolution of a SPP_{air}-WG avoided crossing with the d_{SiO_2} thickness shown in figure 2. For d_{SiO_2} =100 nm (first row in the figure) the upper and the lower curves of the crossing are located above and below the SP resonance at $\hbar\omega_{sp}^{Au}$=2.384 eV. For thicker SiO_2 layers the WG modes and the avoided crossings migrate to lower energy and several new SPP_{air}-WG crossings become visible.

3.2 Evolution of the SPP_{air}-WG avoided crossings with the SiO_2 thickness

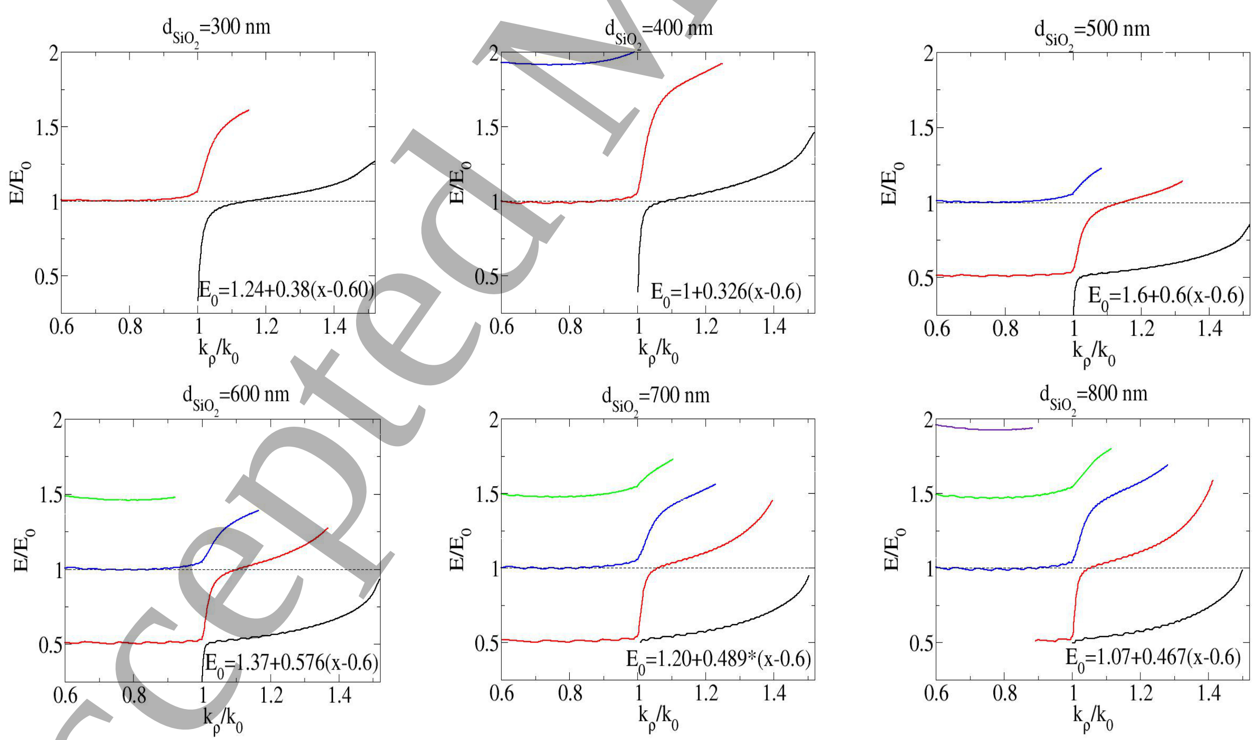

Figure 4: The coupled dispersion curves of the avoided crossings for a thickness d_{Au}=25 nm. The black-red, red-blue and blue-green curves represent the dispersion of the SPP_{air}-WG_1, SPP_{air}-WG_2 and a third (not discussed) avoided crossings. Novotny's model [44] has been used to subtract a linear variation E_0 from the background of the raw curves of the avoided crossing (parameters given at the bottom right corner of each panel). Curves obtained from the minima of the reflectance of the 3D graphs of figure 2.

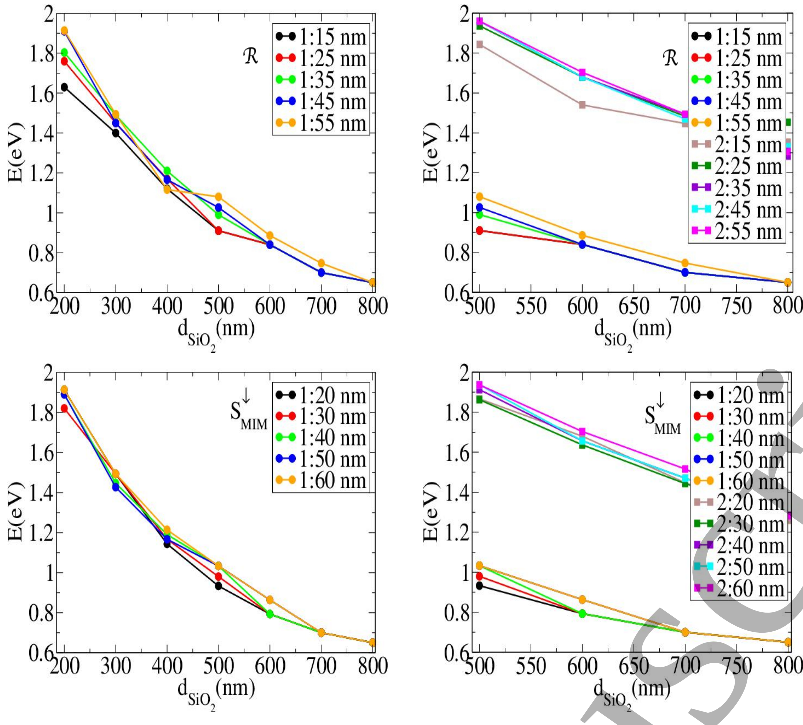

Figure 5: The position of the SPP_{air}-WG_1 avoided crossing (left column) and of the first SPP_{air}-WG_1 (1:d_{Au} nm; symbol •) and the second SPP_{air}-WG_2 (2:d_{Au} nm; symbol ■) crossings (right column). The first and second row panels correspond to calculations using the reflectance $\mathcal{R}$ and the transmitted flux intensity $S^{\downarrow}$.

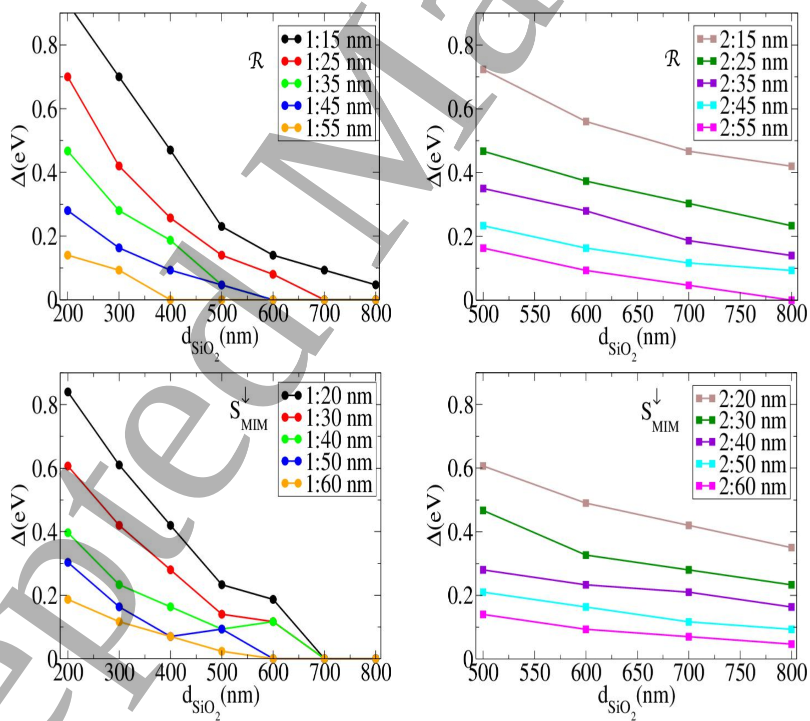

Figure 6: Rabi splitting of the SPP_{air}-WG_i modes avoided crossing of the first WG_1 (left column; 1:d_{Au} nm; symbol •) and of the second WG_2 modes (right column; 2:d_{Au} nm; symbol ■). Same explanations as in figure 5.

To analyze the avoided crossings presented in the 3D plots of figure 2 we have retained two particular crossings SPP_{air}-WG_1 and SPP_{air}-WG_2 corresponding to WG modes with the number of nodes ℓ=1 and ℓ=2, respectively. The 2D dispersion curves in figure 4 were obtained from the minimum of the reflectance $\mathcal{R}$ of the 3D plots presented in figure 2. The background is subtracted form the presented plots using Novotny's avoided crossing model [44]. The left and middle panels of the first row of figure 4 (thickness

$d_{\mathrm{SiO_2}} \in [300, 400]$ nm) show that the $\mathrm{WG_1}$ mode has migrated below the SP resonance frequency at $\hbar\omega$=2.384 eV and its signature becomes visible in the dispersion curves. The other panels of the figure with $d_{\mathrm{SiO_2}} \in$[500,800] nm show that a second, third, and so on WG_i mode, and the associated $\mathrm{SPP_{air}}$-WG_i avoided crossings migrate, to lower energies. This behavior corresponds to the results of Au-$\mathrm{SiO_2}$-Au model of section A.2.

Figure 5 presents the energy positions of the $\mathrm{SPP_{air}}$-$\mathrm{WG_1}$ and $\mathrm{SPP_{air}}$-$\mathrm{WG_2}$ avoided crossings: in the left column the $\mathrm{SPP_{air}}$-$\mathrm{WG_1}$ and in the right column the $\mathrm{SPP_{air}}$-$\mathrm{WG_1}$ and $\mathrm{SPP_{air}}$-$\mathrm{WG_2}$ obtained using the reflectance $\mathcal{R}$ (first row) and the transmitted flux intensity $S^{\downarrow}$ (second row). One sees that the position of the avoided crossing is weakly dependent on the gold thickness and a particular avoided crossing position decreases with increasing $\mathrm{SiO_2}$ thickness. Figure 6, organized in a similar way as figure 5 above, presents the avoided crossing interaction or the Rabi splitting Δ. As a function of the $d_{\mathrm{SiO_2}}$ thickness, the Rabi splitting Δ decreases but, contrary to the position of the avoided crossing, this splitting is much more sensitive to the gold thickness related to the leakage.

Unexpectedly, the left and right columns of figures 5 and 6 show that at different $d_{\mathrm{SiO_2}}$ thicknesses $\mathrm{SPP_{air}}$-$\mathrm{WG_1}$ and $\mathrm{SPP_{air}}$-$\mathrm{WG_2}$ avoided crossings can be close in position and Rabi splitting. For example for E=1.8 eV $\mathrm{SPP_{air}}$-$\mathrm{WG_1}$ and $\mathrm{SPP_{air}}$-$\mathrm{WG_2}$ avoided crossings appear at $d_{\mathrm{SiO_2}}$=230 and 560 nm respectively. Also for the Rabi splitting of Δ=0.6 eV the respective thickness of the two avoided crossings is $d_{\mathrm{SiO_2}}$=300 and 500 nm. The origin of this remarkable coincidence will be discussed in the next section.

3.3 Localization and characterization of the modes

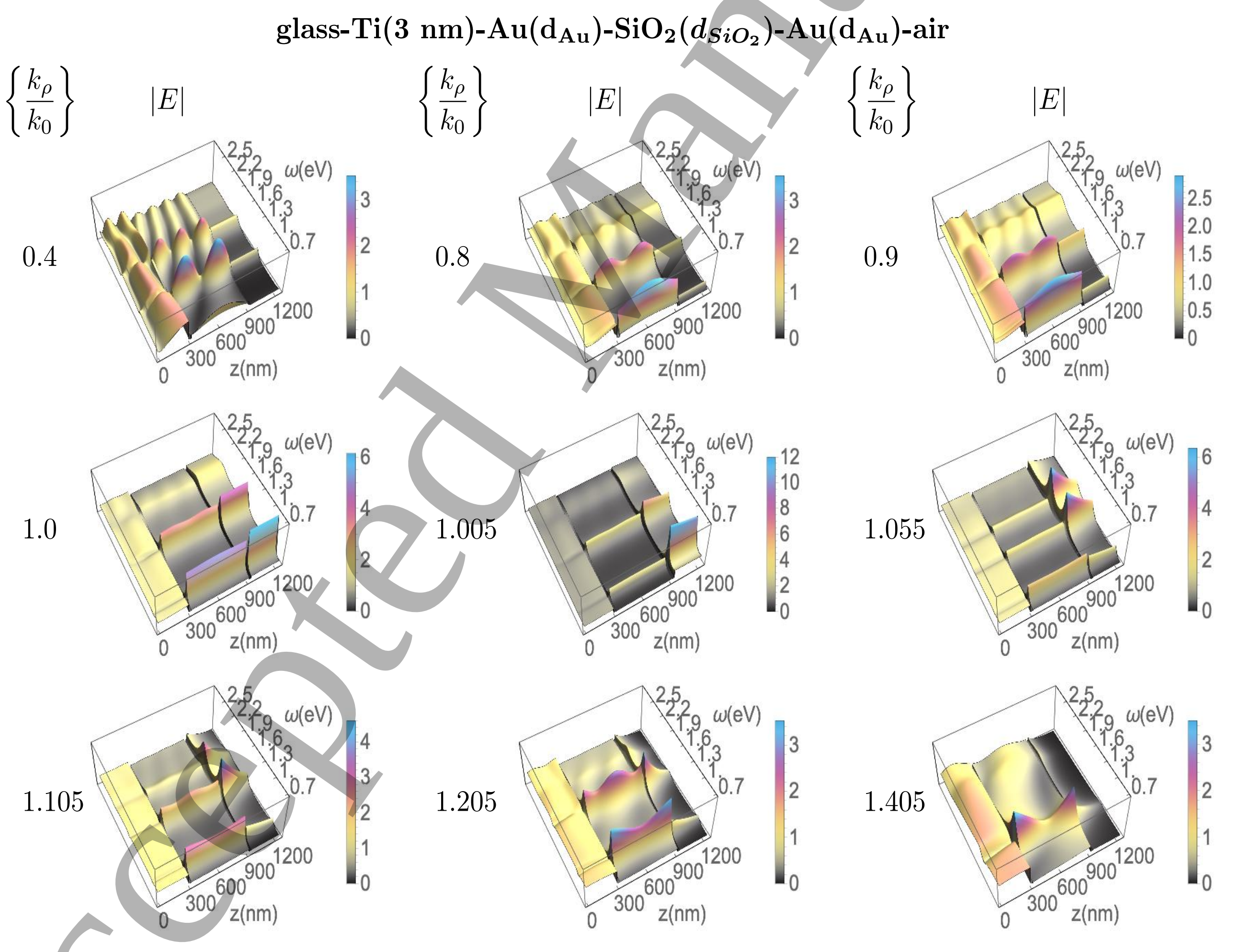

Figure 7: Modulus of the electric field $|E|$ (arbitrary units) function of the penetration coordinate z and of the laser frequency for a glass-Ti-Au(25nm)-$\mathrm{SiO_2}$(600nm)-Au(25nm)-air stack. In the calculation the cladding, with the thickness of 300 nm, is located at: i) cover $z_{\mathrm{glass}} \in [0, 300]$ nm and ii) substrate $z_{\mathrm{air}} \in [900, 1200]$ nm.

The characterization of plasmonic SPP and photonic WG modes can be performed studying the field function of the penetration coordinate z. In the literature this field characterization is performed in different ways: i) Dionne *et al.* [13, 19] and Refki *et al.* [31] use a normalized electric field, ii) Smith *et al.* [18] time averaged electric and magnetic fields and their in-plane or out-of-plane projections, iii) Chen *et al.* [27] the magnetic and the electric fields, and finally iv) Dithbacher *et al.* [12] and Choudhurry *et al.* [22] use the square of the electric and the magnetic fields.

Here we will analyze the properties of the electric field modulus $|E|$ as a function of the penetration coordinate z obtained using an algorithm detailed in the PhD of Achlan [28, chapter 5] or in Cao *et al.* [25, appendix C]). Under a local excitation, in the evanescent region the transmitted flux $S^{\downarrow}$ is expressed in terms of the transmitted coefficients $t^{(\mathfrak{p})}_{n1}$ of a glass-Ti-Au-SiO_2-Au-air stack (see third row of eq. (2)). Thus, we will calculate the modulus of the electric field $|E|$ of this stack excited by an electromagnetic plane wave.

For a selection of in-plane wave vectors k_ρ/k_0 of a stack with d_{SiO_2}=600 nm sustaining several WG modes, figure 7 presents the modulus of the field amplitude $|E|$ as a function of the penetration coordinate z and of the photon energy:

- The first three panels of the figure present the electric field in the allowed region for $k_\rho/k_0 \in [0.4, 0.9]$. The amplitude of the field is $\sim$3, the field modulus is mainly localized in the SiO_2 layer and the WG modes are easily identified having an increasing number of nodes. In air ($z \in [900, 1200]$ nm) one sees a SPP_{air} mode of low amplitude weakly coupling with the WG modes.

- The next four panels of the figure present the forbidden or evanescent region for $k_\rho/k_0 \in [1.0, 1.105]$. Here the electric field of the SPP_{air} mode is dominant in the gold layer and in air ($z \in [900, 1200]$ nm) with an amplitude as high as 12. The mixed SPP_{air}-WG modes of the avoided crossing is clearly visible.

- In the last two panels of the figure corresponding to $k_\rho/k_0 \geqslant 1.105$ the intensity of the electric field drops back down to $\sim$3 and the ratio $|E_{SPP_{air}}|/|E_{WG}|$ of the amplitudes falls continuously. For a large in-plane wave vector $k_\rho/k_0 = 1.405$ only the low frequency WG mode has a significant amplitude.

- In all the 3D graphs of figure 7 one identifies weak features of different shapes in the glass ($z \in [0, 300]$ nm); these are probably a manifestation of the tail of the SPP_{glass} mode that is otherwise forbidden below k_ρ/k_0=1.52.

Now let us discuss the coincidence of the position and strength of the avoided crossing at different d_{SiO_2} thicknesses identified in the preceding section. Recall that the SPP_{air} mode is identical for the two avoided crossings. Since it appears at smaller SiO_2 thicknesses the WG_1 mode has fewer ℓ nodes and compensations of positive and negative contributions to the avoided crossing interaction than the WG_2 mode. Consequently, contrary to the observation, one would expect always a larger interaction in WG_1-SPP_{air} avoided crossing than in WG_2-SPP_{air} one. Figure 7 shows that the electric field of the WG modes is located in the SiO_2 layer whereas that of the SPP_{air} mode is located at the gold-air interface and in air, i.e. in different regions of space. Consequently, the interaction takes place between the electric fields tails of these modes in a small region of space in the neighborhood of the SiO_2-Au interface. The result is that the characteristics of the avoided crossing are nearly independent of the number of nodes of a WG mode. This explains the observed behavior of the avoided crossing interaction as discussed in the preceding section, i.e. similar positions and Rabi splittings for two avoided crossings located at different SiO_2 thicknesses.

To summarize, in agreement with the avoided crossing properties presented in figures 5 and 6 of the preceding section and the behavior of the field function of z shown in figure 7 and discussed here, one concludes that for the present thin film stack there is **no one to one correspondence** between the energy position and Rabi splitting of the avoided crossing and the number of nodes ℓ of a WG mode or of the SiO_2 thickness. Hayashi *et al.* [33] have discussed the interaction of the SPP and WG fields tails of a $IMI_1I_2I_3$ stack with fixed geometrical parameters.

3.4 Intensity enhancement of the modes

Figure 2 and the discussion in section 3.1 above showed that the maximum of the transmitted flux intensity $[S^{\downarrow}]_{max}$ (eq. (2)) oscillates between 2 and 8 10^{-6} for $d_{\mathrm{SiO_2}} \in$[300,800] nm. For a curve with a given d_{Au} thickness, the two top panels of the first two columns of figure 8 present the absolute transmitted flux $[S^{\downarrow}]_{\mathrm{max}}$ having a single maximum $[S^{\downarrow}]_{\mathrm{max}} \approx 8\ 10^{-6}$ at about $\hbar\omega$=1.75 eV. The maxima were obtained relative to the $\mathrm{SiO_2}$ thickness and the in-plane wave vector k_ρ/k_0.

Is this absolute transmitted flux strong or weak? A meaningful estimation of a possible enhancement is obtained by calculating the ratio I_{ref} where ref is either aAug or aSiO2g corresponding to three layer stacks air-Au-glass or air-$\mathrm{SiO_2}$-glass (see details of I_{ref} calculation in section 2.1, eq. (3)). The last two rows of the first two columns of figure 8 show, at about 1.85 eV, an enhancement in the relative fluxes as high as $I_{\mathrm{aAug}} \sim$12 and $I_{\mathrm{aSiO_2g}} \sim$22. As for the absolute flux this maximum is relative to the $\mathrm{SiO_2}$ thickness and the in-plane wave vector k_ρ/k_0.

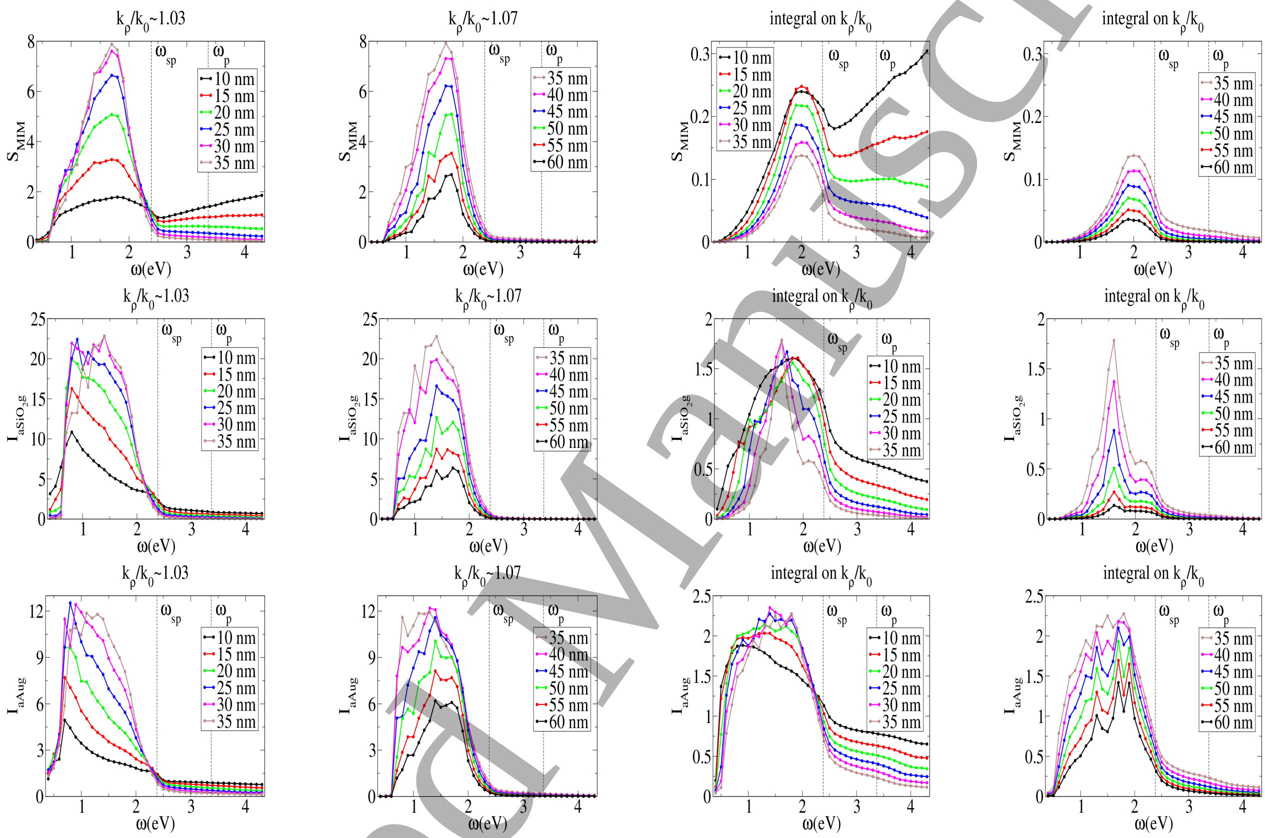

Figure 8: Maxima of the absolute transmitted flux intensity $[S^{\downarrow}]_{max} * 10^6$ (first row, eq. (2)) and of the ratios of the fluxes of our MIM stack $S^{\downarrow}$ and a reference stack $S^{\downarrow}_{ref}$ (second and third rows, eq.(3)). The first two columns of the figure correspond to the intensity maximum obtained relative to the in-plane wave vector k_ρ/k_0 and thickness $d_{\mathrm{SiO_2}}$. The last two columns presenting EM-LDOS are obtained by first integrating over the in-plane vector k_ρ/k_0 then the EM-LDOS maximum is obtained relative to the thickness of $\mathrm{SiO_2}$.

The last two columns of the figure present graphs related to the EM-LDOS. In this case the absolute and relative fluxes were integrated over the in-plane wave vector k_ρ/k_0 and the maximum flux was obtained relative to the $\mathrm{SiO_2}$ thickness only. The rows correspond to the same fluxes $[S^{\downarrow}]_{\mathrm{max}}$, I_{aAug} and $I_{\mathrm{aSiO_2g}}$ where the maxima appear at a frequency between 1.75 and 2 eV for an enhancement factor of between 2 and 2.5.

A similar estimation of the enhancement in the thin film MIM stack composed of air-Ag(40nm)-$\mathrm{MgF_2}$(50nm)-$\mathrm{Alq_3}$(20nm)-$\mathrm{MgF_2}$(50nm)-Ag(200nm)-glass was used by Hayashi *et al.* [23]. Compared to a silver free dielectric stack enhancements of about 25 or 2.5 were found respectively for a particular measurement direction or an integrated over the ejection angle intensities.

The origin of the enhancement in our MIM stack can be either a leaky SPP mode, briefly discussed in section 2.2 above and in appendix A.1, or the avoided crossings between SPP and WG modes analyzed in section 3.2 above:

- In section A.1 figures A-1 and A-2 present the dispersion curves at an air-Au interface in the complex k_ρ/k_0 and k_z/k_0 planes, respectively. The second row of these figures presents the leakage on the proper/improper Riemann sheet function of $\mathrm{Im}[k_\rho/k_0]$ and $\mathrm{Im}[k_z/k_0]$. Below the SP resonance frequency $\omega_{sp}^{\mathrm{Au}}$=2.384 eV this leakage is extremely low and the leaky states can not be responsible for the significant rise of the flux amplitude displayed in figure 8. At higher frequencies, in the QB and RPP regions, the leaky character is pronounced but, as explained in sections 3.1 and B, in these spectral regions the transmitted flux amplitude $S^{\downarrow}$ is extremely low.

- Sections 3.1 and 3.2 show that the $\mathrm{SPP_{air}}$-WGs modes avoided crossings occur in the region of the observables enhancement presented in figure 8 and could be responsible for the rise of the amplitude in the observables. In agreement with the amplitude rise in figure 8, between 1.4 and 2.0 eV figures 2 and B-2 show that the SPP_{air}-WGs avoided crossings give rise to a transmitted flux amplitude $S^{\downarrow}$ enhancement with the maximum as high as 8 10^{-6}.

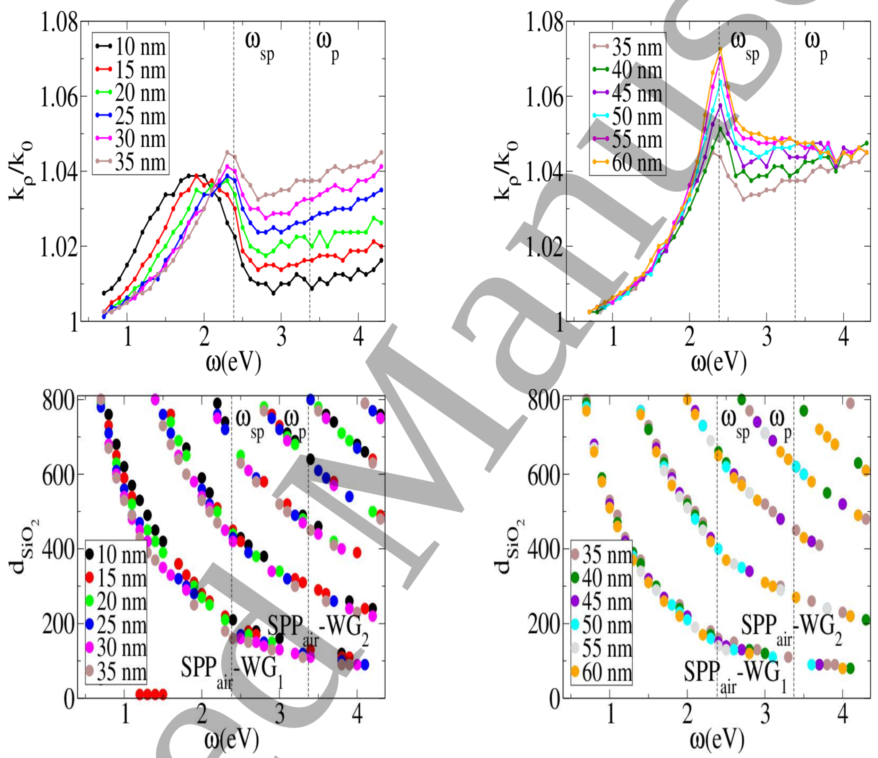

Figure 9: The first and second row of the figure present plots of the in-plane wave vector k_ρ/k_0 and of the thickness $d_{\mathrm{SiO_2}}$ as a function of the energy.

- First row of figure 9 presents the values of the in-plane wave vector $\{k_\rho/k_0\}^{max}$ as a function of the laser frequency ω. The results are obtained using the transmitted flux maximum $[S^{\downarrow}]_{max}$ shown in the first two panels (left-side) of figure 8. For a gold thickness d_{Au} ⩽35 nm (left panel) and d_{Au} >35 nm (right panel) the in-plane wave vector is $\{k_\rho/k_0\}^{max}$ ≈1.03 and $\{k_\rho/k_0\}^{max}$ ≈1.07 respectively. These in-plane wave vector values are close to the position of the SPP_{air} mode or to the location of the $\mathrm{SPP_{air}}$-WG avoided crossing. As a result, the most probable origin of the enhancement are the avoided crossings.

The panels of the second row of figure 9 display $d_{\mathrm{SiO_2}}/\omega$ dependence of the Poynting vector intensity maximum $[S^{\downarrow}]_{max}$ of figure 8 above. Several sets of points close to each other form parallel curves with similar slopes. A curve corresponds to a particular avoided crossing migrating from the high frequency low $\mathrm{SiO_2}$ thickness to the low frequency high $\mathrm{SiO_2}$ thickness. Precisely, as labeled in the figure, the first lowest two curves correspond to the avoided crossings $\mathrm{SPP_{air}}$-$\mathrm{WG_1}$ and $\mathrm{SPP_{air}}$-$\mathrm{WG_2}$ discussed in section

3.2 above whereas the higher curves correspond to other avoided crossings appearing in the MIM stack. As for the dispersion curves of the preceding sections, for $[S^{\downarrow}]_{max}$ the presented curves are again the signature of the multi valued relation between the thickness of the SiO_2 and the properties (position, Rabi splitting) of the SPP_{air}-WG avoided crossing already discussed above.

4 Conclusion

The present theoretical study of a MIM asymmetric six layer air-Au-SiO_2-Au-Ti-glass thin film stack was motivated by an experimental and theoretical paper we have recently published (Cao *et al.* [25]) where we have explored a reduced set of parameters of this stack. In this paper one covers a wider range of SiO_2 ($d_{SiO_2} \in$[0,800] nm) and Au ($d_{Au} \in$[0,60] nm) thicknesses, excitation frequencies ($\hbar\omega$(eV) $\in$[0.7,4.3]) and in-plane wave vectors ($k_\rho/k_0 \in$[0,1.52]). To our knowledge such a study has not been performed up to now. Our idea was to find sets of geometrical parameters and variables where the observables are enhanced. If confirmed experimentally, these sets would permit the development of new applications: sensors, plasmonic circuitry, wave guiding etc.

First, at least for this MIM stack, the region where the observables enhancement takes place is situated below the SP resonance at ω_{sp}=2.384 eV. To fulfill the constraints of an usual experiment the in-plane wave vector is restricted to $k_\rho/k_0 \leqslant$1.52. Consequently only the SPP_{air} but not the SPP_{glass} will contribute to the observable. Secondly, we showed that the enhancement in the observables is due to avoided crossings of the plasmonic SPP_{air} mode with several photonic WG modes located in the SiO_2 dielectric and not to the leaky character of the SPP mode which is extremely low. The enhancement of the transmitted flux intensity of our MIM stack relative to an air-Au-glass or air-SiO_2-glass reference stack is respectively I_{aAug} **∼12 times** or I_{aSiO_2g} **∼22**. When integrated over the light emission angle the enhancement of the flux related to the EM-LDOS is respectively about **2** or **2.5** times larger than the reference stack. Measuring the photoluminescience in an air-Ag-MgF_2-Alq_3-MgF_2-Ag MIM stack Hayashi *et al.* [23] also found a similar enhancements of 25 and 2.5 times relative to a stack without any metal whereas Yang *et al.* [17] found a few percent enhancement in air-Au-SiO_2-Al_2O_3-SiO_2-Au-air compared to a stack with only SiO_2. Thirdly, the localization of the SPP_{air} mode at the air-Au interface and in air and of the WG mode in the SiO_2 film gives rise to a SPP_{air}-WG interaction between the respective electric field tails. Consequently the avoided crossing position and Rabi splitting is weakly dependent on the number of nodes ℓ of a WG mode or of the SiO_2 thickness. Therefore the Rabi splitting **can be large** for WG modes having several nodes ℓ or for stacks with a large SiO_2 thickness. It results that the present MIM stack is of versatile nature since at a given frequency several SiO_2 thicknesses can generate enhancements suitable for applications.

For particular a set of geometrical parameters, energies and in-plane wave vector projection, the results presented in this work display an enhancement but no Fano resonance has been identified. This resonance, having an extremely steep slope of interest in bio sensors, was invoked in avoided crossings implying IMI (see introduction and refs. [33, 9]) or MIM stacks (see the introduction and refs. [36, 16]). These authors showed that a Fano resonance appears in stacks with an excessively weak SPP-WG interaction. For our stack this corresponds to large d_{SiO_2} and d_{Au} thicknesses and a low photon frequency. Since an extremely small in-plane wave vector k_ρ/k_0 mesh is needed to find such a feature it is possible that it has been omitted in the present calculation. We hope to tackle this Fano resonance in a future work.

In the present paper a MIM stack based on gold was studied but, as stated in the introduction, the majority of the literature uses silver [2, 31] or silver and gold [14]. Figures A-1 and A-2 show that at metal-dielectric interfaces gold and silver have different dispersion curves. In gold the dispersion curves of the SPP_{air} and SPP_{glass} modes are nearly parallel to the light lines. If one extends k_ρ/k_0 beyond 1.52 of our preceding experimental work (Cao *et al.* [25]) the qualitative behavior of the SPP_{air} mode presented in this work will probably not change. Studies beyond k_ρ/k_0=1.52 are necessary to confirm this hypothesis. The situation is different in the MIM stacks with silver since the SPP_{air} and SPP_{glass} dispersion curves sweep and cross over the range of k_ρ/k_0 from 0 to above 1.52. Would the SPP_{air}-WGs avoided crossings dispersion curves be qualitatively changed by the sweeping of the SPP_{glass} mode? To answer this question studies on silver MIM thin film stacks have to be performed in the extended range of the in-plane wave vector k_ρ/k_0 when covering the SPP, QB and RPP spectral regions. This will permit to have a global view of the behavior of plasmonic metal thin film stacks.

A Dispersion relations of modes in simple stacks

A.1 Plasmonic SPP mode dispersion at a single metal-dielectric interface

In this section we present the dispersion curves of two plasmonic Au-dielectric and Ag-dielectric interfaces. The idea is to study the behavior of the Au-dielectric interface constituent of the studied six layer stack in the main text and also to compare Au-dielectric and Ag-dielectric interfaces in order to obtain some general trends of the most commonly used plasmonic metals.

Recall that at a single metal-dielectric interface plasmon polariton (PP) modes cover the SPP, QB and RPP spectral regions defined in section 2.2 of the main text. At a single interface the dispersion expressions of a PP mode are well documented (see e.g. Raether [45, appendix 1], Maier [1])

$$k_\rho^{pp} = k_0\sqrt{\frac{\varepsilon_m\,\varepsilon_d}{\varepsilon_m+\varepsilon_d}} = \mathrm{Re}[k_\rho^{pp}] + i\,\mathrm{Im}[k_\rho^{pp}]$$

$$\mathrm{Re}[k_\rho^{pp}] = k_0\sqrt{\frac{\varepsilon_d\,\varepsilon_m^r}{\varepsilon_d+\varepsilon_m^r}} \qquad \mathrm{Im}[k_\rho^{pp}] = \pm k_0\frac{\varepsilon_m^i}{2(\varepsilon_m^r)^2}\left(\frac{\varepsilon_m^r\,\varepsilon_d}{\varepsilon_m^r+\varepsilon_d}\right)^{3/2} \tag{A-1}$$

where k_ρ^{pp} is the in-plane wave vector projection (see figure 1, where the cylindrical frame in the coordinate space is shown), $k_0 = (\omega/c)$ the vacuum wave vector and ε_m and ε_d are the metal and dielectric permittivities. The out-of-plane wave vector projection k_z reads

$$k_{zi} = \pm\sqrt{k_i^2 - k_\rho^2}, \tag{A-2}$$

where i designates the layer of the out-of-plane projection. The above wave vector projections have branch points of order 2 in the complex k_ρ and $k_{zi} \equiv k_z$ planes (see e.g. Ishimaru [46, chap. 3]). These planes are divided into two Riemann sheets: a *proper/top* sheet with $\mathrm{Im}[k_\rho] > 0$ or $\mathrm{Im}[k_z] > 0$ and an *improper/bottom* sheet with $\mathrm{Im}[k_\rho] < 0$ or $\mathrm{Im}[k_z] < 0$.

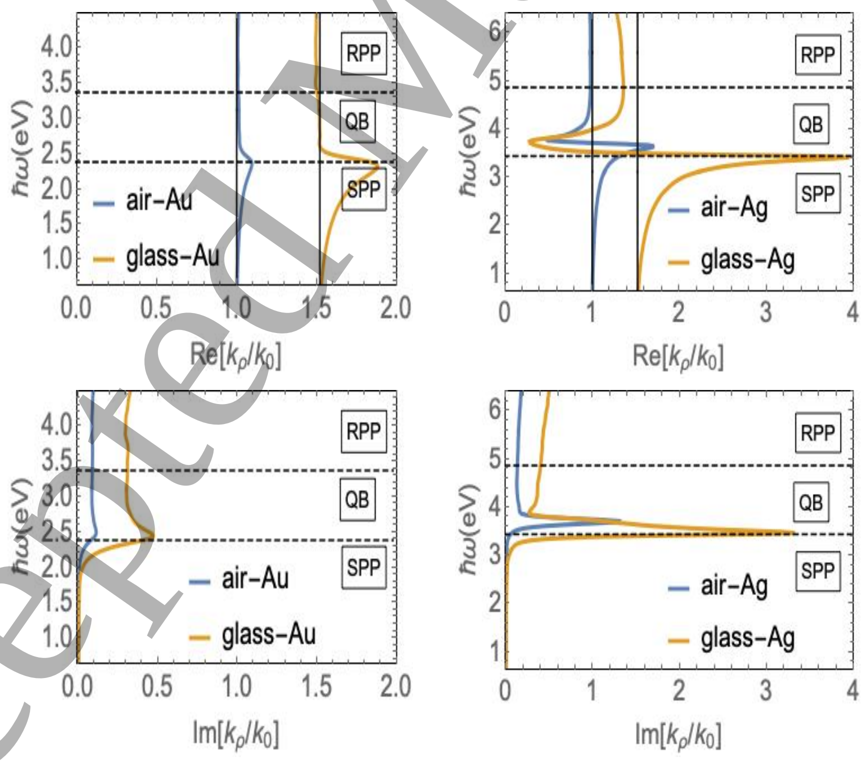

Figure A-1: Dispersion of plasmon polariton (PP) modes (eq. (A-1)) at air/Me and glass/Me interfaces, where Me=Au and Ag. The dispersion and leakage (proper Riemann sheet, abscissa $\mathrm{Im}[k_\rho/k_0] > 0$) are displayed in the first and second row of the figure. The vertical lines in the graphs of the first row are the light lines. The horizontal dashed lines correspond to the SP resonance $\omega_{sp}^{\mathrm{Au}}$=2.384 eV and $\omega_{sp}^{\mathrm{Ag}}$= 3.44 eV and to the RPP resonance $\omega_{rpp}^{\mathrm{Au}}$=3.3715 eV and $\omega_{rpp}^{\mathrm{Ag}}$=4.8649 eV calculated using the experimental material functions of Johnson and Christy [47].

The first row of figure A-1[1] presents the dispersion of the PP mode at the air/Me and glass/Me interfaces with Me=Au, Ag. The SPP_{air} and SPP_{glass} plasmonic modes appear slightly above the vertical dielectric light lines at $\mathrm{Re}[k_\rho/k_0 \equiv n_{air}]$=1.0 and $\mathrm{Re}[k_\rho/k_0 \equiv n_{glass}]$=1.52. The dashed horizontal lines in the figure give the energy position of the SP and the RPP resonances (the numerical values are given in the figure caption). In gold the two PP^{Au}_{air} and PP^{Au}_{glass} modes closely follow the light lines whereas in silver below the SP resonance the dispersion curves sweep over the entire range of $\mathrm{Re}[k_\rho/k_0]$ and above this resonance sweeps and crosses (first row left and right panels in the figure).

The second row of figure A-1 displays the leakage (proper Riemann sheet) of the PP mode. Two regions can be distinguished: i) below the SP resonance ω_{sp} $\mathrm{Im}[k_\rho/k_0]< 0.1$ is small implying a low attenuation/enhancement (proper/improper Riemann sheet) and ii) near and above ω_{sp} an attenuation/enhancement of the observable becomes significant.

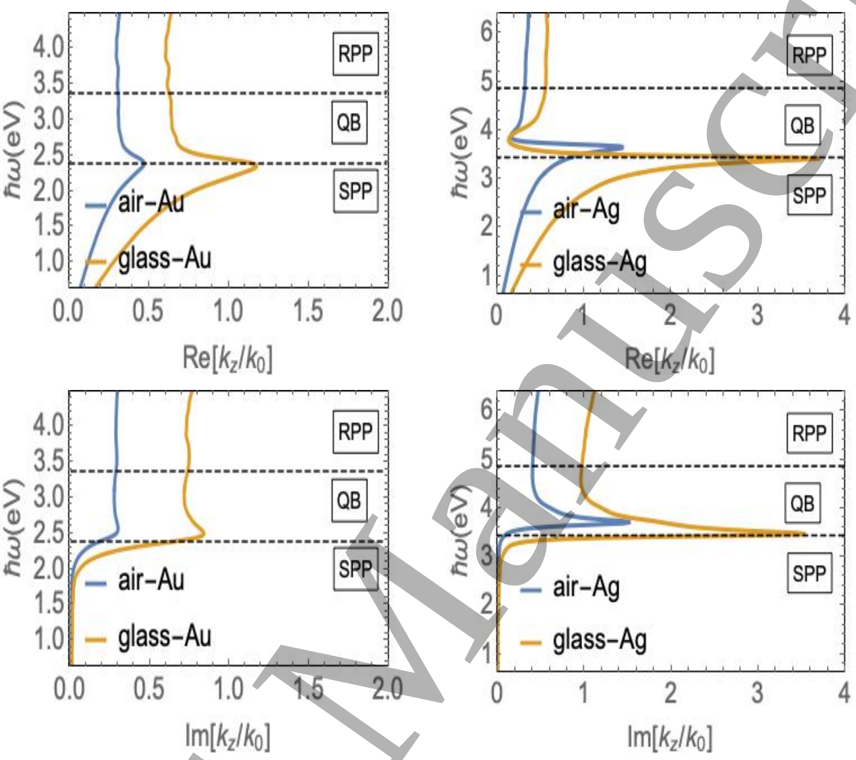

Figure A-2: Dispersion of the out-of-plane wave vector projection k_z (eq. (A-2) giving $k_{z\,i}$) of a PP mode at air/Me and glass/Me interfaces, where Me=Au and Ag. Same notations, abbreviations and material functions as in figure A-1.

Figure A-2 presents the dispersion relation of the out-of-plane wave vector projection $\mathrm{Re}[k_z/k_0]$ (first row) and the corresponding leakage/enhancement $\mathrm{Im}[k_z/k_0]$ on a proper/improper Riemann sheet (second row). One notes a behavior similar to the in-plane wave vector graphs in figure A-1.

In conclusion, globally the in-plane and the out-of-plane wave vector projections in gold and silver display similar behavior. However a closer inspection reveals that for the gold PP_{air} and PP_{glass} curves closely follow the light lines whereas in silver they sweep over the abscissa at low frequencies and both sweep and cross above. Would this difference influence the dispersion curves of a MIM Ag-I-Ag multilayer thin film stack? Only detailed calculations of such silver stacks as the one performed here for gold can answer this question.

A.2 Photonic WG modes dispersion in a three layers MIM stack

Let us discuss a simple planar MIM wave guide Au-SiO_2-Au to model the WG modes of our MIM thin film stack with θ_{SiO_2} the angle of the rays propagating in the guide measured from the normal to the wave

[1] In the textbooks on plasmons (see e.g. Maier [1]) one uses ω/k_ρ and ω/k_z representation of the dispersion where the coordinates are linearly dependent. Here one uses linearly independent $\omega/(k_\rho/k_0)$ and $\omega/(k_z/k_0)$ representation common in radio frequency (see e.g. Hanson and Yakovlev [48]).

guide boundary (Saleh and Teich [43, fig. 7.2-1]). If the condition for real refractive indices $n^r_{\mathrm{Au}} < n_{\mathrm{SiO_2}}$ is satisfied, this Au-SiO$_2$-Au stack will sustain WG modes. Rays making an angle $\theta > \theta_c = \sin^{-1}(n^r_{\mathrm{Au}}/n_{\mathrm{SiO_2}})$, where θ_c is the critical angle of the total reflection, are guided in the SiO$_2$ wave guide. Consider a

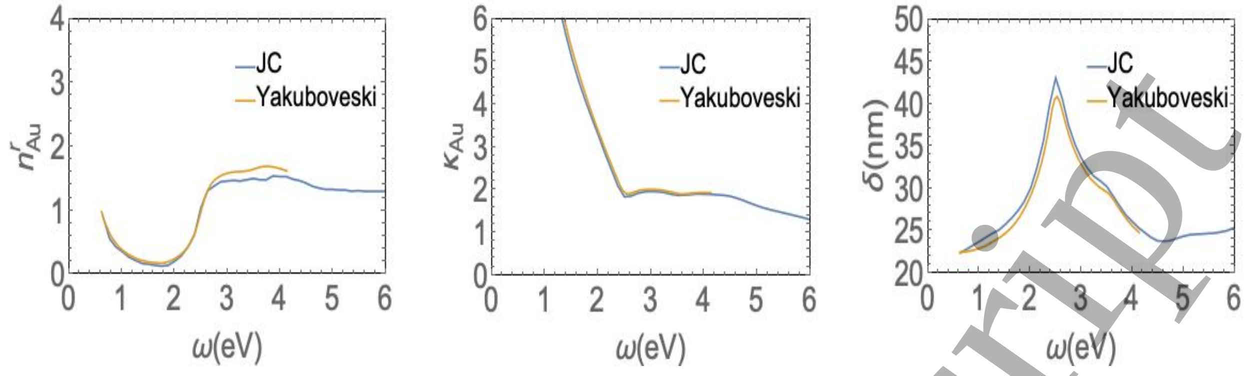

Figure A-3: Experimental refractive indices n^r_{Au}=Re[n$_{\mathrm{Au}}$] and κ_{Au}=Im[n$_{\mathrm{Au}}$] and the skin depth δ(nm) of gold function of the laser frequency. The experimental material functions of Johnson and Christy [47] and Yakubovski *et al.* [49] are shown.

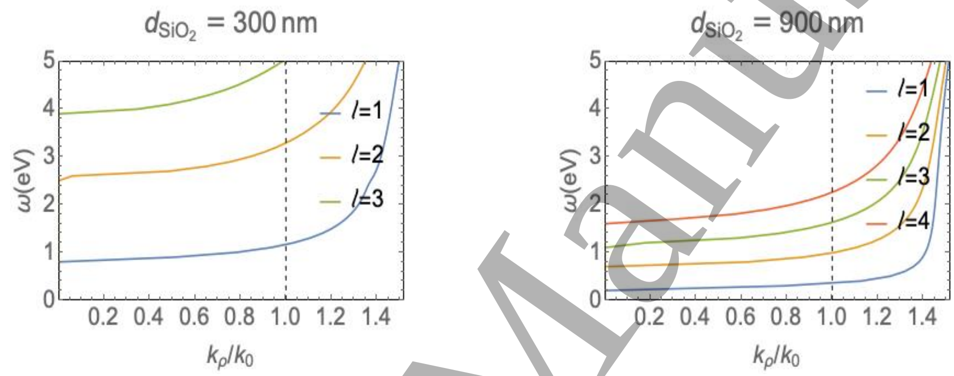

Figure A-4: Dispersion of the modes of a Au-SiO$_2$-Au stack for different ℓ solutions of eq. (A-3). Vertical dashed line separates the allowed $\theta < \theta_c$ and the forbidden or evanescent $\theta > \theta_c$ regions. Two thickness $d_{\mathrm{SiO_2}}$=300 and 900 nm are shown.

simplified accumulated phase (APh) model (see e.g. Saleh and Teich [43, section 7.2]). The existence condition of a mode requires that the accumulated phase at the boundary be mod(2π)

$$2\,\frac{\omega}{c}\,n_{\mathrm{SiO_2}}\,d_{\mathrm{SiO_2}}\,\cos\theta_{\mathrm{SiO_2}} - 2\,\varphi_z = 2\pi\,\ell; \qquad \ell = 0, 1, 2, \ldots \tag{A-3}$$

where ω, $n_{\mathrm{SiO_2}}$ and $d_{\mathrm{SiO_2}}$ are the vacuum angular frequency, the SiO$_2$ refractive index and the thickness of the SiO$_2$ layer. An approximate expression of the phase change φ_z at the SiO$_2$-Au interface is defined in Saleh and Teich [43, eq. (6.2-11)]. Here this phase φ_z is calculated as the argument of the reflection coefficient $r^{(\mathfrak{p})}$ of a ($\mathfrak{p}$)/TM polarized light

$$r^{(\mathfrak{p})} = \frac{n_{\mathrm{Au}}\,\cos\theta_{\mathrm{SiO_2}} - n_{\mathrm{SiO_2}}\cos\theta_{\mathrm{Au}}}{n_{\mathrm{Au}}\,\cos\theta_{\mathrm{SiO_2}} + n_{\mathrm{SiO_2}}\cos\theta_{\mathrm{Au}}} \qquad \tan\varphi_z = \frac{\mathrm{Im}(r^{(\mathfrak{p})})}{\mathrm{Re}(r^{(\mathfrak{p})})}, \tag{A-4}$$

where $n_{\mathrm{Au}} = n^r_{\mathrm{Au}} + i\,\kappa_{\mathrm{Au}}$ is the complex refractive index of gold. Now from eq. (A-3) one obtains the incident angle $\theta_{\mathrm{SiO_2}}$

$$\theta^{\ell}_{\mathrm{SiO_2}} = \cos^{-1}\left(\frac{c}{\omega}\frac{\pi\,\ell + \varphi_z}{n_{\mathrm{SiO_2}}\,d_{\mathrm{SiO_2}}}\right) \qquad \ell = 0, 1, 2, \ldots \tag{A-5}$$

Since the angle $\theta^{\ell}_{\mathrm{SiO_2}}$ and the phase φ_z are a function of each other, for each ℓ the angle $\theta^{\ell}_{\mathrm{SiO_2}}$ is obtained iteratively: (i) start by calculating zero order angle $\theta^{\ell}_{\mathrm{SiO_2}}$ using eq. (A-5) with φ_z set to zero; (ii) calculate φ_z using equations (A-4) with this angle $\theta^{\ell}_{\mathrm{SiO_2}}$; (iii) iterate to convergence.

The in-plane wave vector k_ρ^ℓ parallel to the interfaces needed in the dispersion calculations reads

$$k_\rho^\ell = \frac{\omega}{c}\, n_{\mathrm{SiO_2}} \sin\theta_{\mathrm{SiO_2}}^\ell. \tag{A-6}$$

As stated in the beginning of this section, the appearance condition for the WG modes is $n_{\mathrm{Au}}^r < n_{\mathrm{SiO_2}}$ (Saleh and Teich [43, sec. 7.2]). The refractive index of SiO_2 oscillates between 1.45 and 1.52. Comparing the real part of the refractive index of gold n_{Au}^r, given in the left panel of figure A-3, with $\mathrm{n_{SiO_2}}$ one sees that the WG appearance condition $n_{\mathrm{Au}}^r < n_{\mathrm{SiO_2}}$ is fulfilled approximately in the energy region $\hbar\omega(\mathrm{eV}) \in [0.65, 2.5]$.

Figure A-4 shows the WG mode dispersion curves for several ℓ at two SiO_2 thicknesses, 300 and 900 nm. In the energy region of interest for our studies the number of modes per energy unit rises with the increase in the SiO_2 thickness and a particular WG mode energy position decrease when $d_{\mathrm{SiO_2}}$ increases. Moreover in the allowed region ($k_\rho/k_0 < 1$) the WG mode is nearly independent of the frequency ω permitting a visual identification of the WG modes in the plots.

B Observables in the entire optical domain: SPP, QB and RPP regions

The top 3D representation of the reflectance $\mathcal{R}$ of a glass-Ti(3 nm)-Au-SiO_2-Au-air thin film stack excited by a source at infinity in the optical domain $\hbar\omega(\mathrm{eV}) \in [0.7 - 4.3]$ is presented in figure B-1. For this observable the modes appear as minima in the reflectance (blue color in the graphics). In the same spectral region, the results of the transmitted flux intensity $S^\downarrow$ of an air-Au-SiO_2-Au-Ti-glass thin film stack excited by an oscillating dipole $\vec{\mathrm{p}}_{0z}$ located a few nanometers above the surface are presented in figure B-2 where the modes appear as maxima (blue and red colors).

The optical domain $\hbar\omega(\mathrm{eV}) \in [0.7 - 4.3]$ presented in figures B-1 and B-2 covers all the spectral regions SPP, QB and RPP introduced in section 2.2 of the main text. The analysis of the these figures clearly shows that above the frequency of the SP resonance at 2.384 eV:

- The reflectance $\mathcal{R}$ plateau falls from about 0.8 to 0.4 and the dip minimum in the reflectance is extremely shallow giving rise to modes which are practically indistinguishable.
- The transmitted flux intensity $S^\downarrow$ maximum also falls and the mode becomes so weak that it is difficult to identify. The first column of figure B-2 with d_{Au}=15 nm and $d_{\mathrm{SiO_2}}$ ∈[100,300] nm displays a very luminous background of 0.5 intensity where the modes are difficult to identify.

In summary in the region above the SP resonance at 2.384 eV the amplitude of the modes in the observables is very weak and barely distinguishable from the background. Therefore these spectral domains are excluded from our analysis in the main text where we restrict our study to a region slightly wider than the SPP spectral region, namely $\hbar\omega(\mathrm{eV})$ ∈[0.7,2.8].

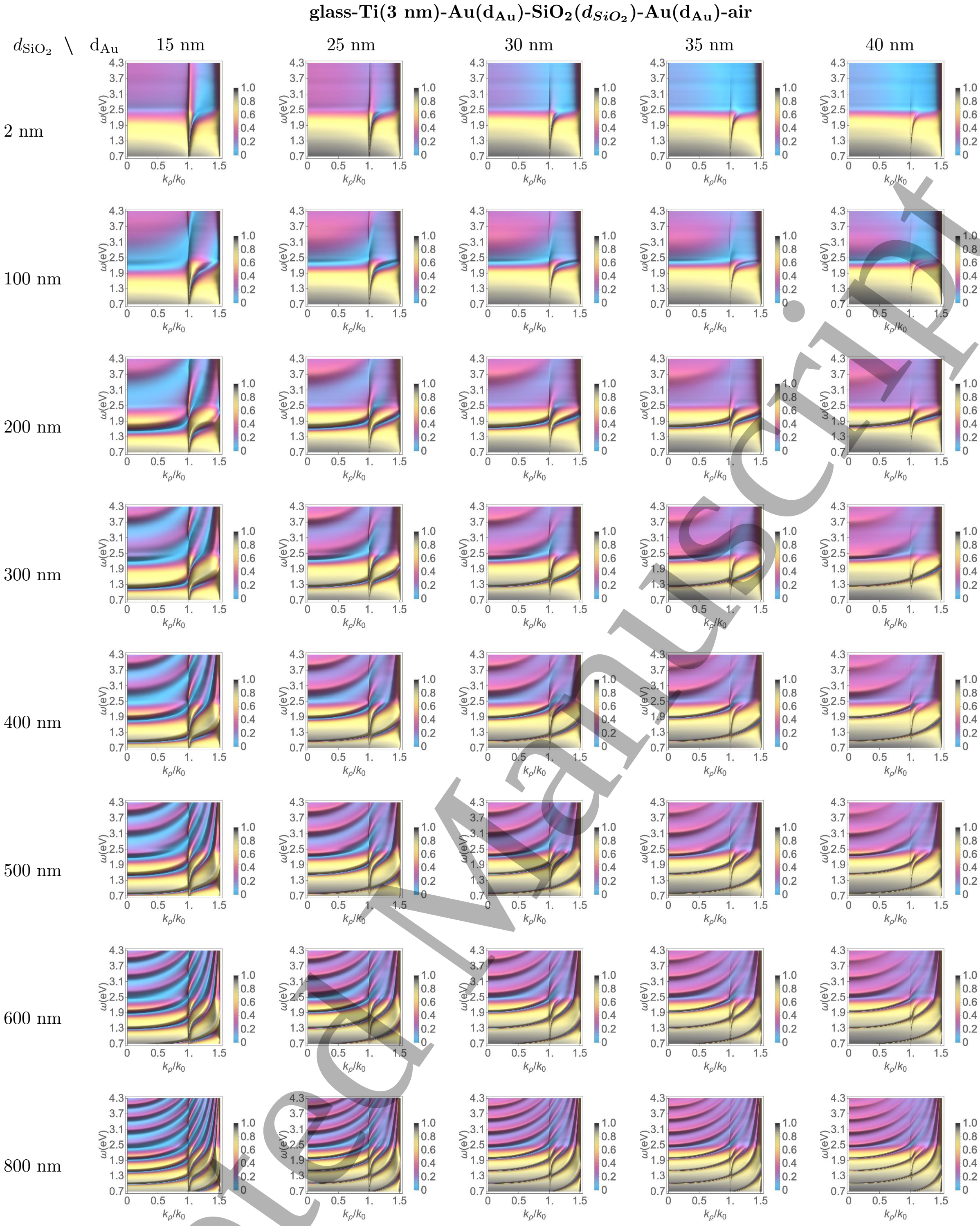

Figure B-1: Top view of the 3D plots of the MIM thin film stack reflectance $\mathcal{R}$ eq. (1) in the frequency region $\hbar\omega(\mathrm{eV}) \in [0.7, 4.3]$ and the in-plane wave vector $k_\rho/k_0 \in [0, 1.52]$. Rows and columns correspond to the SiO$_2$ and Au thicknesses respectively $d_{\mathrm{SiO_2}}$ and d_{Au}. The SPP, QB and RPP regions introduced in section 2.2 can be identified.

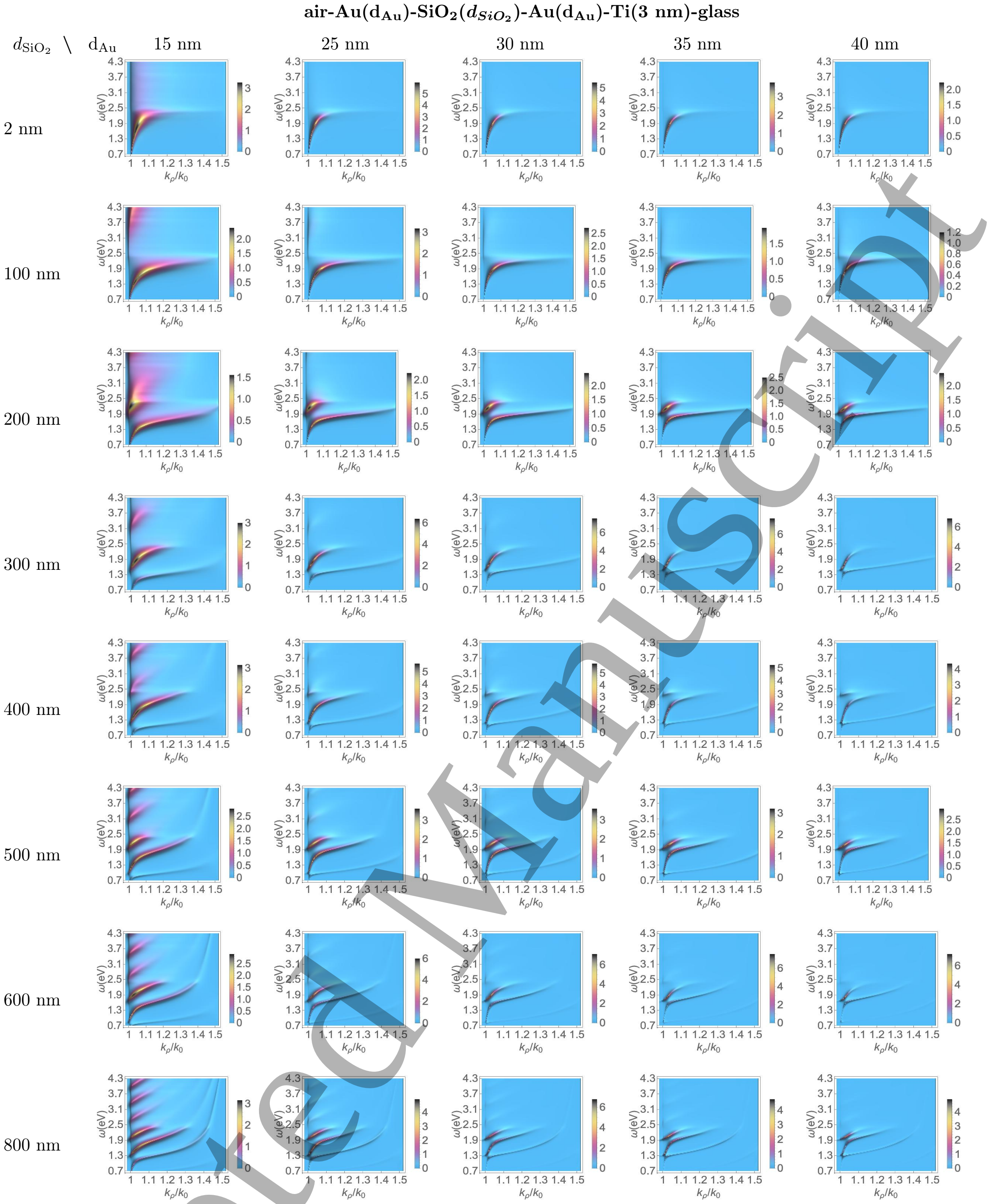

Figure B-2: Top view of the 3D plots of the MIM thin film stack transmitted flux intensity $S^{\downarrow}$ (eq. (2), intensity multiplied by 10^6) in the frequency region $\hbar\omega(\text{eV}) \in [0.7, 4.3]$ and the in-plane wave vector $k_\rho/k_0 \in [1, 1.52]$. Same labeling as in figure B-1.

Funding:
Moustafa Achlan acknowledges the Alumini Association of the Libanese University's Faculty of Sciences (Tripoli, Lebanon) for a Ph.D fellowship.

Acknowledgments:
We acknowledge constructive exchanges with Eric Le Moal and Elizabeth Boer-Duchemin, our experimental collaborators, during this theoretical work and the preparation of the manuscript. We acknowledge Andrew J. Mayne for the continuous scientific exchanges and encouragements during this work and for the critical reading of the manuscript.

References

[1] S. A. Maier, Plasmonics: Fundamentals and applications, Springer, New York, 2007.

[2] S. Hayashi, T. Okamoto, Plasmonics: visit the past to know the future, Journal of Physics D: Applied Physics 45 (43) (2012) 433001.
URL `http://stacks.iop.org/0022-3727/45/i=43/a=433001`

[3] Z. Han, S. I. Bozhevolnyi, Radiation guiding with Surface Plasmon Polaritons, Reports on Progress in Physics 76 (1) (2013) 016402. doi:10.1088/0034-4885/76/1/016402.
URL `https://doi.org/10.1088%2F0034-4885%2F76%2F1%2F016402`

[4] Z. Han, S. I. Bozhevolnyi, Chapter 5 - Waveguiding with Surface Plasmon Polaritons, in: N. Richardson, S. Holloway (Eds.), Modern Plasmonics, Vol. 4 of Handbook of Surface Science, North-Holland, 2014, pp. 137 – 187. doi:https://doi.org/10.1016/B978-0-444-59526-3.00005-7.
URL `http://www.sciencedirect.com/science/article/pii/B9780444595263000057`

[5] E. Verhagen, J. A. Dionne, L. K. Kuipers, H. A. Atwater, A. Polman, Near-field visualization of strongly confined surface plasmon polaritons in metal−insulator−metal waveguides, Nano Letters 8 (9) (2008) 2925–2929, pMID: 18690753. arXiv:https://doi.org/10.1021/nl801781g, doi:10.1021/nl801781g.
URL `https://doi.org/10.1021/nl801781g`

[6] H. Lu, H. Xiong, Z. Huang, Y. Li, H. Dong, D. He, J. Dong, H. Guan, W. Qiu, X. Zhang, W. Zhu, J. Yu, Y. Luo, J. Zhang, Z. Chen, Electron-plasmon interaction on lithium niobate with gold nanolayer and its field distribution dependent modulation, Opt. Express 27 (14) (2019) 19852–19863. doi:10.1364/OE.27.019852.
URL `http://www.opticsexpress.org/abstract.cfm?URI=oe-27-14-19852`

[7] J. Homola, Surface plasmon resonance sensors for detection of chemical and biological species, Chemical Reviews 108 (2) (2008) 462–493, pMID: 18229953. arXiv:https://doi.org/10.1021/cr068107d, doi:10.1021/cr068107d.
URL `https://doi.org/10.1021/cr068107d`

[8] L. Yang, J. Wang, L.-z. Yang, Z.-D. Hu, X. Wu, G. Zheng, Long-range surface plasmons polaritons, Scientific Reports 8 (2018) 2560. doi:10.1038/s41598-018-20952-7.
URL `https://doi.org/10.1038/s41598-018-20952-7`

[9] Y. Li, Y. Yuan, X. Peng, J. Song, J. Liu, J. Qu, An ultrasensitive Fano resonance biosensor using two dimensional hexagonal boron nitride nanosheets: theoretical analysis, RSC Adv. 9 (2019) 29805–29812. doi:10.1039/C9RA05125B.
URL `http://dx.doi.org/10.1039/C9RA05125B`

[10] B. Ruan, Q. You, J. Zhu, L. Wu, J. Guo, X. Dai, Y. Xiang, Fano resonance in double waveguides with graphene for ultrasensitive biosensor, Opt. Express 26 (13) (2018) 16884–16892. doi:10.1364/OE.26.016884.
URL `http://www.opticsexpress.org/abstract.cfm?URI=oe-26-13-16884`

[11] S. Hayashi, Y. Fujiwara, B. Kang, M. Fujii, D. V. Nesterenko, Z. Sekkat, Line shape engineering of sharp Fano resonance in Al-based metal-dielectric multilayer structure, Journal of Applied Physics 122 (16) (2017) 163103. arXiv:https://doi.org/10.1063/1.5002715, doi:10.1063/1.5002715.
URL `https://doi.org/10.1063/1.5002715`

[12] H. Ditlbacher, N. Galler, D. Koller, A. Hohenau, A. Leitner, F. Aussenegg, J. Krenn, Coupling dielectric waveguide modes to surface plasmon polaritons, Opt. Express 16 (14) (2008) 10455–10464. doi:10.1364/OE.16.010455.
URL `http://www.opticsexpress.org/abstract.cfm?URI=oe-16-14-10455`

[13] J. A. Dionne, L. A. Sweatlock, H. A. Atwater, A. Polman, Planar metal plasmon waveguides: frequency-dependent dispersion, propagation, localization, and loss beyond the free electron model, Phys. Rev. B 72 (2005) 075405. doi:10.1103/PhysRevB.72.075405.
URL `http://link.aps.org/doi/10.1103/PhysRevB.72.075405`

[14] S. Refki, S. Hayashi, H. Ishitobi, D. V. Nesterenko, A. Rahmouni, Y. Inouye, Z. Sekkat, Resolution enhancement of plasmonic sensors by metal-insulator-metal structures, Annalen der Physik 530 (4) (2018) 1700411. arXiv:https://onlinelibrary.wiley.com/doi/pdf/10.1002/andp.201700411, doi:10.1002/andp.201700411.
URL https://onlinelibrary.wiley.com/doi/abs/10.1002/andp.201700411

[15] J. Vlček, J. Pištora, M. Lesňák, Design of plasmonic-waveguiding structures for sensor applications, Adv. Optics Photonics 9 (9) (2019) 1227. doi:10.3390/nano9091227.

[16] Y. Neo, T. Matsumoto, T. Watanabe, M. Tomita, H. Mimura, Transformation from plasmon-induced transparence to -induced absorption through the control of coupling strength in metal-insulator-metal structure, Opt. Express 24 (23) (2016) 26201–26208. doi:10.1364/OE.24.026201.
URL http://www.opticsexpress.org/abstract.cfm?URI=oe-24-23-26201

[17] H. Yang, J. Li, G. Xiao, Significantly increased surface plasmon polariton mode excitation using a multilayer insulation structure in a metal-insulator-metal plasmonic waveguide, Appl. Opt. 53 (17) (2014) 3642–3646. doi:10.1364/AO.53.003642.

[18] L. Smith, M. Taylor, I. Hooper, W. Barnes, Field profiles of coupled surface plasmon-polaritons, J. Modern Opt. 55 (2008) 2929–2943. doi:10.1080./09500340802271250.

[19] J. A. Dionne, L. A. Sweatlock, H. A. Atwater, A. Polman, Plasmon slot waveguides: Towards chip-scale propagation with subwavelength-scale localization, Phys. Rev. B 73 (2006) 035407. doi:10.1103/PhysRevB.73.035407.
URL https://link.aps.org/doi/10.1103/PhysRevB.73.035407

[20] C. Symonds, C. Bonnand, J. C. Plenet, A. Bréhier, R. Parashkov, J. S. Lauret, E. Deleporte, J. Bellessa, Particularities of surface plasmon–exciton strong coupling with large Rabi splitting, New Journal of Physics 10 (6) (2008) 065017.
URL http://stacks.iop.org/1367-2630/10/i=6/a=065017

[21] Z. Sekkat, S. Hayashi, D. V. Nesterenko, A. Rahmouni, S. Refki, H. Ishitobi, Y. Inouye, S. Kawata, Plasmonic coupled modes in metal-dielectric multilayer structures: Fano resonance and giant field enhancement, Opt. Express 24 (18) (2016) 20080–20088. doi:10.1364/OE.24.020080.
URL http://www.opticsexpress.org/abstract.cfm?URI=oe-24-18-20080

[22] S. Choudhury, R. Badugu, J. Lakowicz, Directing fluorescence with plasmonic and photonic structures., Acc. Chem. Res. 48 (2015) 2171–2180. doi:10.1021/acs.accounts.5b00100.

[23] S. Hayashi, A. Maekawa, S. C. Kim, M. Fujii, Mechanism of enhanced light emission from an emitting layer embedded in metal-insulator-metal structures, Phys. Rev. B 82 (2010) 035441. doi:10.1103/PhysRevB.82.035441.
URL https://link.aps.org/doi/10.1103/PhysRevB.82.035441

[24] H. Saito, K. Namura, M. Suzuki, H. Kurata, Dispersion relations for coupled surface plasmon-polariton modes excited in multilayer structures, Microscopy 63 (1) (2014) 85–93. doi:10.1093/jmicro/dft047.
URL http://dx.doi.org/10.1093/jmicro/dft047

[25] S. Cao, M. Achlan, J.-F. Bryche, P. Gogol, G. Dujardin, G. Raşeev, E. L. Moal, E. Boer-Duchemin, An electrically induced probe of the modes of a plasmonic multilayer stack, Opt. Express 27 (23) (2019) 33011–33026. doi:10.1364/OE.27.033011.
URL http://www.opticsexpress.org/abstract.cfm?URI=oe-27-23-33011

[26] Y. Kurokawa, H. T. Miyazaki, Metal-insulator-metal plasmon nanocavities: Analysis of optical properties, Phys. Rev. B 75 (2007) 035411. doi:10.1103/PhysRevB.75.035411.
URL https://link.aps.org/doi/10.1103/PhysRevB.75.035411

[27] J. Chen, G. A. Smolyakov, S. R. J. Brueck, K. J. Malloy, Surface plasmon modes of finite, planar, metal-insulator-metal plasmonic waveguides, Opt. Express 16 (19) (2008) 14902–14909. doi:10.1364/OE.16.014902.
URL http://www.opticsexpress.org/abstract.cfm?URI=oe-16-19-14902

[28] M. Achlan, Surface plasmons polariton and wave guide modes in a six layer thin film stack, Ph.D. thesis, Université de Paris-Sud, Orsay, France (2018).

[29] S. Hayashi, D. V. Nesterenko, Z. Sekkat, Fano resonance and plasmon-induced transparencyin waveguide-coupled surface plasmon resonance sensors, Applied Physics Express 8 (2015) 022201. URL http://dx.doi.org/10.7567/APEX.8.022201

[30] S. Hayashi, D. V. Nesterenko, A. Rahmouni, Z. Sekkat, Observation of Fano line shapes arising from coupling between surface plasmon polariton and waveguide modes, Applied Physics Letters 108 (5) (2016) 051101. arXiv:https://doi.org/10.1063/1.4940984, doi:10.1063/1.4940984. URL https://doi.org/10.1063/1.4940984

[31] S. Refki, S. Hayashi, A. Rahmouni, D. Nesterenko, Z. Sekkat, Anticrossing behaviour of surface plasmon polariton dispersions in metal-insulator-metal structures, Plasmonics (2016) 433–440doi:10.1007/s11468-015-0047-7.

[32] S. Hayashi, D. V. Nesterenko, A. Rahmouni, H. Ishitobi, Y. Inouye, S. Kawata, Z. Sekkat, Light-tunable Fano resonance in metal-dielectric multilayer structures, Scientific Reports 6 (2016) 33144. doi:10.1038/srep3314. URL https://doi.org/10.1038/srep33144

[33] S. Hayashi, D. V. Nesterenko, , Z. Sekkat, Waveguide-coupled surface plasmon resonance sensor structures: Fano lineshape engineering for ultrahigh-resolution sensing, Journal of Physics D: Applied Physics 48 (32) (2015) 325303. doi:10.1088/0022-3727/48/32/325303. URL https://doi.org/10.1088%2F0022-3727%2F48%2F32%2F325303

[34] D. V. Nesterenko, S. Hayashi, Z. Sekkat, Extremely narrow resonances, giant sensitivity and field enhancement in low-loss waveguide sensors, Journal of Optics 18 (6) (2016) 065004. doi:10.1088/2040-8978/18/6/065004. URL https://doi.org/10.1088%2F2040-8978%2F18%2F6%2F065004

[35] D. Koller, A. Hohenau, H. Ditlbacher, N. Galler, F. Reil, F. Aussenegg, A. Leitner, E. List, J. Krenn, Organic plasmon-emitting diode, Nature Photonics 2 (2008) 684–687. doi:10.1038/nphoton.2008.200. URL https://doi.org/10.1038/nphoton.2008.200

[36] K. Matsunaga, T. Watanabe, Y. Neo, T. Matsumoto, M. Tomita, Attenuated total reflection response to wavelength tuning of plasmon-induced transparency in a metal–insulator–metal structure, Opt. Lett. 41 (22) (2016) 5274–5277. doi:10.1364/OL.41.005274. URL http://ol.osa.org/abstract.cfm?URI=ol-41-22-5274

[37] P. Yeh, Optical Waves in Layered Media, Wiley Series in Pure and Applied Optics, Wiley, New York, 2005.

[38] D. Bethune, Optical harmonic generation and mixing in multilayer media: analysis using optical transfer matrix techniques, J. Opt. Soc. Am. B 6 (1989) 910–916.

[39] W. Lukosz, R. Kunz, Light emission by electric and magnetic dipoles close to a planar interface. I. Total radiated power, J.Opt. Soc. Am. 67 (1977) 1607–1615.

[40] L. Novotny, Allowed and forbidden light in near-field optics. I. A single dipolar light source, J. Opt. Soc. Am. A 14 (1) (1997) 91–104. doi:10.1364/JOSAA.14.000091. URL http://josaa.osa.org/abstract.cfm?URI=josaa-14-1-91

[41] L. Novotny, B. Hecht, Principles of Nano-Optics, Cambridge University Press, Cambridge, 2006.

[42] P. Bharadwaj, A. Bouhelier, L. Novotny, Electrical excitation of surface plasmons, Phys. Rev. Lett. 106 (2011) 226802. doi:10.1103/PhysRevLett.106.226802. URL https://link.aps.org/doi/10.1103/PhysRevLett.106.226802

[43] B. Saleh, M. Teich, Fundamental of Photonics, Wiley Series of Pure and Applied Physics, John Wiley & Sons, Inc, New York, 1991.

[44] L. Novotny, Strong coupling, energy splitting, and level crossings: A classical perspective, American Journal of Physics 78 (11) (2010) 1199–1202. arXiv:https://doi.org/10.1119/1.3471177, doi:10.1119/1.3471177.
URL `https://doi.org/10.1119/1.3471177`

[45] H. Raether, Surface plasmons on smooth and rough surfaces and on grating, Springer-Verlag, Berlin, 1988, editor: G. Hohler.

[46] A. Ishimaru, Electromagnetic wave propagation, radiation and scattering. From fundamentals to applications, IEEE Press, Wiley, New York, 2017.

[47] P. B. Johnson, R. W. Christy, Optical constants of the noble metals, Phys. Rev. B 6 (12) (1972) 4370–4379. doi:10.1103/PhysRevB.6.4370.

[48] G. W. Hanson, A. Yakovlev, Investigation of mode interaction on planar dielectric wave guides with loss and gain, Radio Sci. 34 (6) (1999) 1349–1359.

[49] D. I. Yakubovsky, A. V. Arsenin, Y. V. Stebunov, D. Y. Fedyanin, V. S. Volkov, Optical constants and structural properties of thin gold films, Opt. Express 25 (21) (2017) 25574–25587. doi:10.1364/OE.25.025574.
URL `http://www.opticsexpress.org/abstract.cfm?URI=oe-25-21-25574`